

# UNCLASSIFIED

AD NUMBER
AD864764
NEW LIMITATION CHANGE
TO Approved for public release, distribution unlimited
FROM Distribution authorized to U.S. Gov't. agencies and their contractors; Administrative/Operational Use; 1969. Other requests shall be referred to Naval Air Systems Command, Washington, DC 20360.
AUTHORITY
Naval Air Systems Command ltr dtd 26 Oct 1971

THIS PAGE IS UNCLASSIFIED

MICROSTRUCTURE STUDIES OF REFRACTORY

POLYCRYSTALLINE OXIDES

SUMMARY REPORT

25 June 1969 to 24 December 1969

Contract N00019-69-C-0198

AVSD-0038-70-RR

Prepared for

U.S. Naval Air Systems  
Washington 25, D.C.

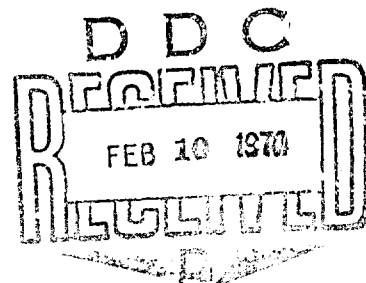
Prepared by

W.H. Rhodes  
R.M. Cannon

Reproduced by the  
CLEARINGHOUSE  
for Federal Scientific & Technical  
Information Springfield Va. 22151

AVCO CORPORATION  
Systems Division  
Lowell, Massachusetts 01851

THIS DOCUMENT IS SUBJECT TO SPECIAL EXPORT  
CONTROLS AND FORTH TRANSMITTAL TO FOREIGN GOVERN-  
MENTS OR FOR COPIES THEREOF MAY BE MADE ONLY WITH  
THE PRIOR APPROVAL OF COMMANDER, NAVAL AIR SYSTEMS  
COMMAND, AIR 6024 WASHINGTON, D.C. 20360



Best Available Copy

MICROSTRUCTURE STUDIES OF REFRACTORY

POLYCRYSTALLINE OXIDES

SUMMARY REPORT

25 June 1969 to 24 December 1969

Contract N00019-69-C-0198

AVSD-0038-70-RR

Prepared for

U.S. Naval Air Systems  
Washington 25, D.C.

Approved by

*T. Vasilos*

T. Vasilos

Prepared by

W.H. Rhodes  
R.M. Cannon

AVCO CORPORATION  
Systems Division  
Lowell, Massachusetts 01851

THIS DOCUMENT IS SUBJECT TO SPECIAL EXPORT  
CONTROLS AND IS NOT TO BE DISTRIBUTED OUTSIDE THE GOVERNMENT  
UNLESS AUTHORIZED BY THE COMMISSIONER OF CUSTOMS AND BORDER  
PROTECTION, U.S. DEPARTMENT OF COMMERCE, WASHINGTON, D.C. 20540

TABLE OF CONTENTS

FOREWORD	viii
ABSTRACT	ix
I. INTRODUCTION	1
II. DEFORMATION OF HIGH PURITY ALUMINA	1
A. General	1
B. Material and Procedure	3
1. Raw Material	3
2. Test Procedure	3
C. Results and Discussion	4
1. Chemical Characterization	4
2. Consolidation	6
3. Deformation Behavior	8
a. Analysis	8
b. Test Results	10
c. Comparison of Two Alumina Bodies	18
d. Microstructure Study	21
e. Discussion of the Comparison Between Alumina Bodies	28
f. Discussion of Deformation at High Strains	30
4. Fracture Strength	32
D. Summary	32
III. PRESS FORGING ALUMINA	34
A. General	34
B. Material and Procedure	35
C. Results and Discussion	35

TABLE OF CONTENTS (Concl'd)

1. Crystallographic Texture	38
2. High Density Forging	40
3. Influence of Temperature on Forging	41
4. Rapid Deformation-Quenching Experiment	47
5. Mechanical Properties	47
D. Summary	50
IV. STRESS CORROSION OF MAGNESIUM OXIDE	51
A. General	51
B. Material and Procedure	52
1. Specimen Preparation	52
2. Sample and Test Arrangement	52
C. Results	52
D. Summary	62
V. REFERENCES	64

LIST OF ILLUSTRATIONS

Figure No.

2.1	Ground Surface Showing Starting Microstructure of Test Specimen 1404-6. . . . .	9
2.2	Moment and Stress versus Strain for High Purity Specimen 1404-4 . . . . .	11
2.3	Moment and Stress versus Strain for High Purity Specimen 1358-3 . . . . .	12
2.4	Moment and Stress versus Strain for Change of Strain Rate Test on Specimen 1404-6. . . . .	14
2.5	Steady-State Stress from First 2% Strain versus Strain Rate for High Purity Al <sub>2</sub> O <sub>3</sub> . . . . .	15
2.6	Steady-State Stress from First 2% Strain versus Strain Rate for High Purity Al <sub>2</sub> O <sub>3</sub> at 1400°C . . . . .	16
2.7	Fracture Surface of Specimen 1404-4 after Two Bending Cycles and 9% Strain at 1400°C . . . . .	17
2.8	Strain Rate for 10 Kpsi Flow Stress for High Purity and Standard Alumina . . . . .	19
2.9	Strain Rate - Grain Size Relationship for Three Grades of Al <sub>2</sub> O <sub>3</sub> . . . . .	20
2.10	Activation Energy for Steady-State Creep as a Function of Grain Size for Several Materials. . . . .	22
2.11	Diffusion Coefficients versus Reciprocal Temperature for Several Al <sub>2</sub> O <sub>3</sub> Bodies . . . . .	23
2.12	Product of Boundary Width Times Diffusion Coefficients versus Reciprocal Temperature . . . . .	24
2.13	Surface Structure of Sample 1404-4 Tested at 1400°C . . . . .	25
2.14	Tensile Surface Structure of Sample 1404-1 Tested at 1350°C . . . . .	27
2.15	Compressive Surface of Sample 1358-2 after Second Cycle at 1350°C . . . . .	27
2.16	Tensile Surface of Sample 1358-1 Tested at 1450°C . . . . .	29

LIST OF ILLUSTRATIONS (Cont'd)

Figure No.

2.17	Tensile Surface of Sample 1404-6 Tested at 1400°C. . . . .	29
2.18	Bend Strength as a Function of Temperature. . . . .	33
3.1	Pressure Sintering Apparatus used for Press-Forging Experiments . . . . .	36
3.2	Ratio of Relative X-ray Intensity for Forged, Sintered and Hot Pressed Al <sub>2</sub> O <sub>3</sub> . . . . .	39
3.3	Powder Alumina Forgings at, a) 1650°C - D1282, b) 1740°C - D1240 and c) 1850°C - D1277. . . . .	42
3.4	Microstructure of Several Powder Alumina Forgings at 1750°C. . . . .	43
3.5	Ratio of Relative X-ray Intensity at Center and Rim Position of Forged Billet . . . . .	44
3.6	Ratio of Relative X-ray Intensity for Billets Forged at Three Different Temperatures . . . . .	45
3.7	Microstructure in Dense Region of Rapidly Forged-Quenched Billet 1294 . . . . .	48
3.8	Bend Strength versus Temperature of a Forged Billet Compared to Hot Pressed Material. . . . .	49
4.1	Microstructure of Vacuum Hot Pressed Baker MgO using LiF Process . . . . .	54
4.2	Electron Micrograph of Baker MgO Sample Showing Grain Boundary Phase . . . . .	55
4.3	Higher Magnification View of Grain Boundary Phase in Baker MgO. . . . .	55
4.4	Delayed Failure Curve for Baker MgO Tested in H <sub>2</sub> O and 1 M DMF Compared with Fisher MgO in H <sub>2</sub> O . . . . .	57
4.5	Central Region of MgO Stress Corrosion Sample 112-7 . . . . .	59
4.6	A and B Secondary Crack and Corrosion Features on Grain Face near Tensile Surface of MgO . . . . .	61
4.7	A and B Secondary Crack Features near Tensile Surface of MgO Stress Corrosion Sample 112-8 . . . . .	62

LIST OF TABLESTable No.

2.1	Spark Source Mass Spectrographic Analysis of High Purity $\text{Al}_2\text{O}_3$ . . . . .	5
2.2	Summary of Expected Hot Pressed and Annealed High Purity Alumina Impurity Concentration . .	7
2.3	High Purity Alumina Fabrication . . . . .	8
3.1	$\text{Al}_2\text{O}_3$ Forgings. . . . .	37
3.2	Microstructure Variables on Billets Forged at Varying Temperatures. . . . .	43
4.1	Emission Spectrographic Analysis. . . . .	53
4.2	Base-Line Strength of $\text{MgO}$ . . . . .	57
4.3	Delayed Fracture Test on $\text{MgO}$ . . . . .	59



FOREWORD

This report was prepared by the Applied Technology Division of Avco Corporation under U.S. Navy Contract N00019-69-C-0198, entitled, "Microstructure Studies of Polycrystalline Oxides."

The work was administered under the direction of the U.S. Department of the Navy, Air Systems Command, with Mr. Charles F. Bersch, Code AIR-52032A, acting as Project Engineer.

This report covers work conducted from 25 June 1969 to 24 December 1969.

The writers are pleased to acknowledge the contributions of the following individuals to this program; R. Gardner and P. Fuce for ceramographic preparation, J. Centorino, A. Moses and R. Martineau for materials preparation. P. Burnett and C.L. Houck for electron microscopy, P. Berneburg for x-ray studies, and R.M. Haag, T. Vasilos and J. Niesse for useful discussions.

ABSTRACT

Several facets of the effect of microstructure and chemistry on the mechanical properties of magnesia and alumina were studied. Comparison of the deformation properties of high purity  $\text{Al}_2\text{O}_3$  with a standard research grade of  $\text{Al}_2\text{O}_3 + 1/4\%$  MgO demonstrated high purity material possessed a normalized creep rate approximately a factor of five (5) lower and a higher strain rate sensitivity suggesting an increased importance of diffusional creep. At strains from 3-12% evidence was obtained for strain hardening, a Bauschinger effect and polygonization which suggested considerable dislocation and grain boundary sliding activity. Also, high temperature stress-strain curves showed evidence for blunting a potentially catastrophic failure event.

$\text{Al}_2\text{O}_3$  press forging experiments resulted in a better understanding of deformation and primary recrystallization processes. Bend tests of a uniform 8 micron grain size textured body demonstrated higher elevated temperature strength than 1-2 micron hot pressed  $\text{Al}_2\text{O}_3$  suggesting a real benefit from the textured structure resulting from one of a number of potential models.

Dead load stress corrosion studies on polycrystalline MgO demonstrated that the shape of the stress corrosion curve was dependent on the starting chemistry and/or minor grain boundary phases. Also, the resistance to dead load was markedly influenced by the introduction of 1 molar dimethyl formamide which had been shown to affect dislocation mobility in MgO. The evidence does not unequivocally identify whether a chemical or mechanical model of stress corrosion applies, but it is clear that stress corrosion is a problem which must be recognized in commercial bodies of MgO.

## I. INTRODUCTION

This study covers several facets of the broad topic of microstructure and chemistry effects on mechanical properties of oxide ceramics. The studies have concentrated on two oxides; 1) magnesium oxide because it serves as a model system for isotropic oxides and has several important practical applications to industrial and military needs, and 2) aluminum oxide mainly because it finds such a broad application for industrial and military requirements, but it also is a model anisotropic oxide.

The work is divided into three categories; 1) Deformation studies on high purity alumina. Powders having a reported purity of 99.9995%  $\text{Al}_2\text{O}_3$  were fabricated by vacuum hot pressing to dense 0.8 micron billets. Thorough chemical and microstructural characterization preceded deformation studies up to 12% strain in the 1300-1450°C range. The results are compared with similar studies on 99.9%  $\text{Al}_2\text{O}_3$  + 1/4% MgO. 2) Press forging alumina. Microstructure and crystallographic texture control by press forging techniques was studied. The low and high temperature fracture strengths of uniform 8 micron grain size  $\text{Al}_2\text{O}_3$  + 0.1% MgO were determined, and new information was gained on the operative deformation and recrystallization mechanisms. 3) Stress corrosion of magnesium oxide. Studies were made to determine whether corrosion was intrinsic to polycrystalline MgO or strongly influenced by impurity phases. Also, tests were conducted in 1 M dimethyl formamide which is known to affect dislocation mobility in MgO to determine whether a mechanical or chemical model of stress corrosion applies.

## II. DEFORMATION OF HIGH PURITY ALUMINA

### A. General

There is general agreement that property measurements on single and polycrystalline ceramics have to date reflected extrinsic behavior. Furthermore, the lack of sufficiently pure specimens has made it difficult, if not impossible, to unequivocally separate structure-sensitive from composition-sensitive properties. Properties sensitive to point defects such as electrical conductivity, diffusion and hardness are thought to be particularly sensitive to composition. For example, Aust and Westbrook<sup>(1)</sup> have found that grain boundary hardening is associated with impurity-vacancy interactions. There is considerable evidence that grain growth rates are impurity sensitive. Also, line defects and their response to imposed stress are known to be dependent on impurities. These facts lead one to anticipate an effect of chemical purity on the mechanical properties of oxides. In particular, it is expected that the plastic properties of oxides will most dramatically show the dependence on purity. Consequently, the current effort was a study of the deformation behavior of vacuum hot pressed high purity high density  $\text{Al}_2\text{O}_3$ . For comparison previous results<sup>(2)</sup> on moderate purity (99.9%)  $\text{Al}_2\text{O}_3$  + 1/4 w/o MgO will be introduced and reviewed.

The 1-2 micron grain size  $\text{Al}_2\text{O}_3$  + 1/4 w/o MgO was very ductile in the 1300-1550°C range. The steady-state flow stress was very sensitive to strain rate with values of 0.6 - 0.7 for the strain rate sensitivity,  $m$  in the relation:

$$\sigma = K \dot{\epsilon}^m \quad (1)$$

where  $\sigma$  is the stress,  $\dot{\epsilon}$  the strain rate and K a material constant. A strong grain size dependence fit the relation

$$\dot{\epsilon} \propto \frac{1}{G^{2.5}} \quad (2)$$

where G is the grain size. As much of the earlier<sup>(2,3,4)</sup> work by others had interpreted their results by the Nabarro-Herring diffusional creep relation:

$$\dot{\epsilon} = \frac{13.3 D \nu}{kT G^2} \quad (3)$$

where D is the diffusivity,  $\nu$  is the vacancy volume, and kT have the usual meaning, attempts were made to correlate the behavior for the hot pressed fine grain material with the earlier studies. However, the strain rate dependence for the 1-2  $\mu$ m material clearly indicated a behavior that was distinct from pure diffusional creep. As the grain size of the material was increased up to 5  $\mu$ m (the 5  $\mu$ m material was MgO-free) and then to 10 microns, m values increased to about 0.8 - 0.9 which was taken to indicate a transition to a diffusional creep mechanism.

The deformation mechanism that was thought to dominate at low grain sizes was grain boundary sliding. This was supported by microstructural evidence for displaced triple points. Also, electron microscopy of thin foils showed dislocations at some of the boundaries on which sliding had occurred. It was concluded that the actual boundary sliding process was non-Newtonian ( $m < 1$ ) involving dislocations in some manner. Grain boundary sliding requires some sort of accommodation. This process was not identified, but it probably included diffusional creep and grain boundary migration. Some twinning was seen providing accommodation at points of high stress concentration, i.e., triple points. There was no positive evidence that dislocation slip had contributed to the necessary shape changes.

Very recently on a concurrent program<sup>(5)</sup> this same material was tested in reverse bending with up to 6 cycles and 48% total strain. After the first couple percent of strain a rather strong work hardening was apparent (in the earlier work specimens were only strained to 2%), and the rate of work hardening increased with each cycle. Also, a very strong Bauschinger effect (lower yield stress on reversal of strain than maximum stress at unloading) was found which tended to diminish in magnitude with successive cycles. In addition, a yield phenomena similar to that observed in "strain aging" and the more classic yield drop was occasionally observed. The Bauschinger behavior was partially rationalized in terms of the relief of stresses at triple points and other obstacles to grain boundary sliding upon reversal of this sliding. This work is not yet complete, thus the explanations are tentative and conclusions have not yet been drawn. However, the data is

repeatable and will be checked in the tension and torsion mode. Thus, the work to be reported on high purity  $\text{Al}_2\text{O}_3$  includes the effect of steady-state (within 2%) flow stress on strain rate and behavior on reverse loading at high strains at several temperatures.

## B. Material and Procedure

### 1. Raw Material

One lot of high purity  $\text{Al}_2\text{O}_3$  was employed in this study.\* This lot had been previously<sup>(6,7)</sup> characterized and the fabrication process optimized. The necessary specimens were vacuum hot pressed by the process developed.

### 2. Test Procedure

Samples with different cross-sections (0.050 x 0.125 or 0.030 x 0.070 inches) and 0.875 inches long were tested in 4-point bending. A molybdenum resistance furnace and argon test environment was employed. The bend fixture was constructed from TZM and chemically polished sapphire knife edges were used (extensive testing with a variety of candidate materials demonstrated these to have superior sliding frictional properties). A tungsten strain measuring probe (referenced to the lower knife edge block) was coupled with a LVDT and recorder for strain and strain rate measurements. Considerable care was taken to eliminate spurious loads or bellows friction problems. Both load and deformation were recorded separately versus time. Machined specimens were cleaned in  $\text{HF} \cdot \text{HNO}_3$ ,  $\text{H}_2\text{O}$  and ethanol and handled only with teflon tweezers or while wearing white gloves.

The normal practice was to strain the specimen to the limit of the bend fixture (5% for the 0.050 x 0.125 cross-section and 2.5% for the 0.030 x 0.070 cross section) at a constant strain rate. Several tests were conducted by changing strain rate once steady-state stress (within the 2% limit) was reached. A number of tests were conducted in reverse bending; that is, once the limit of the bend fixture was reached, the specimen was cooled, turned over and again bent to the limit of the device (because of the specimen curvature twice as much strain was obtained during the second and subsequent bending experiments).

Considerable care was taken to monitor microstructural changes after the test. Replica electron microscopy was performed on each specimen before testing, after each cycle on both tension and compression surfaces, and on either the fracture surfaces or a subsurface section (if fracture did not occur). The latter check was only obtained after the final bend of a re-bend specimen. Unstrained control samples were also replicated after each test cycle.

\* Lot S5578 supplied by United Mineral, Distributor for Johnson-Matthey with a reported purity of 99.9995%  $\text{Al}_2\text{O}_3$ .

## C. Results and Discussion

### 1. Chemical Characterization

Over the past several years (6,7) this lot (S5578) of  $Al_2O_3$  has been analyzed by emission spectroscopy, plasma source mass spectroscopy and spark source mass spectroscopy. In this current period spark source mass spectroscopy was used almost exclusively.\* Carbon and fluorine were determined by fusion and wet chemical technique, respectively. One sample which had been previously analyzed was resubmitted as a cross reference to the old analysis. The other samples analyzed were the high purity powder - S5578, a vacuum hot pressed sample produced from this powder - 1368 AP, a bend bar machined from the same high purity sample after having been tested at  $1350^{\circ}C$  - 1368-1, and a vacuum hot pressed sample (using the same precautions as employed for the high purity  $Al_2O_3$ ) produced from Linde A  $Al_2O_3$ . These analyses along with the previous analysis on Sample 1331 are listed in Table 2.1.

Keeping in mind that the reproducibility for mass spectrography is approximately + 50% the agreement between analyses of 1331 is quite good for most elements. However, the discrepancy in the second analysis was considered serious for the following elements: Cu factor of 4 higher, Ni factor of 4 higher, Ca factor of 2 lower, Si factor of 2 higher and Mg factor of 5 lower. Interference with other peaks makes Mg analysis difficult, thus it is thought that the lower Mg figure represents the correct value for both samples. In the case of the other discrepancies it is not known which value to believe. It is apparent from considering the analyses for the other high purity samples that No. 1331 was contaminated at some point in its history. This was the second sample, produced in a new Poco graphite die and as such it may have picked up some impurities from the die. (Care was taken to clean the die and it was outgassed at  $1700^{\circ}C$  prior to use). In any event Sample 1368 which was pressed 7 runs later was a factor of three lower in detected impurities.

The analysis of the S5578 powder and the two 1368 samples exhibit some interesting trends. During hot pressing the following impurities are picked up: K - factor of 3, some Si and Na - factor of 4. These three elements, of course, are very common in our universe and probably just very hard to keep out of any system. (Because the C analysis was done two different ways it is not clear if C is picked up or lost during hot pressing.) It is interesting that some Cl is expelled from the powder during hot pressing and an even greater quantity is lost in the annealing of the individual sample during the high temperature test. It is perhaps equally significant that S and F were not rejected from the system during either hot pressing or the high temperature test cycles.

The analysis of the Linde A derived Sample 1420 was quite interesting in that only 2 times more impurities were detected compared with the high purity sample. The principle differences were; factor of 100 higher B, factor

\* Performed by D.C. Walters and E.R. Blosser, Battelle Memorial Institute, Columbus, Ohio.

TABLE 2.1

SPARK SOURCE MASS SPECTROGRAPHIC

ANALYSIS OF HIGH PURITY Al<sub>2</sub>O<sub>3</sub>

Sample Number and Impurity Concentration in ppmw

Impurity Element	Sample 1331	No. 1331	No. 1368-1	No. 1368-AP	S5578 Powder	No. 1420
Pb	0.2	0.3	0.5	0.1	1	1
Ba	2	1	0.05	0.1	0.1	0.1
Mo	1	1	0.2	0.2	0.2	0.2
Zr	1	1	0.6	0.6	0.2	3
Y	0.1	.1	0.2	.03	.1	.05
Sr	1	0.4	0.1	.1	0.1	0.3
Ca	1	0.3	0.1	0.1	0.1	40
Zn	6.0	6	1	0.6	0.5	0.1
Cu	0.5	2	0.2	0.2	0.6	0.2
Ni	1	4	0.2	0.2	0.2	0.4
Fe	20	30	2	2	3	15
Mn	1	1	0.5	0.5	0.3	0.3
Cr	3	5	ND 0.1	0.1	0.1	0.1
Th	0.6	1	0.2	0.1	1	0.2
Ca	30	15	10	5	5	10
K	30	20	6	6	2	20
Cl	40	70	15	40	50	15
S	10	10	10	10	10	10
P	1	0.4	0.2	.2	.1	0.3
Si	50	100	6	20	15	15
Mg	100	20	10	20	10	2
Na	40	40	40	40	10	100
F	6	10	10	4	4	4
B	3	3	1	2	0.2	20
Li	0.3	0.3	0.04	.02	0.4	0.4
C	NA	NA	NA	NA	800	80.0

of 2 1/2 higher Na, lower Mg, lower Cl, factor of 2 1/2 higher K, factor of 2 higher Ca, factor of 5 higher Fe and 40 ppmw Ga. Thus, this particular powder lot of Linde A was quite pure, and it is apparent that by using careful processing techniques this purity can be maintained.

Basically three techniques have been used over two years to analyze high purity  $Al_2O_3$ . In general, emission spectroscopy showed the S5578 powder to be much higher purity than either of the mass spectroscopy techniques. The precision on the mass spectroscopy technique is quoted to be + 300%, and emission spectroscopists will usually mention a figure of + 200%. Using these figures the authors have reviewed all the analytical work on S5578 alumina over the last 3 years and produced a conservative (with respect to claiming high purity) estimate of the impurity concentration both in the as-hot pressed and annealed condition. These values shown in Table 2.2 total 305 ppm impurities after hot pressing and 120 ppm after a suitable anneal to reduce C, Cl and perhaps F and N. The cation impurity concentration alone was 80 ppm after annealing.

The plasma source mass spectrographic work demonstrated another important fact concerning the chemical nature of this material. Impurities are inhomogeneously dispersed throughout both the powder and the hot pressed sample. This means that it is quite possible to encounter areas that are very clean as well as quite contaminated with respect to the above analysis. Little is known concerning the size or concentration of these pockets.<sup>(8)</sup> This condition is probably quite general in other  $Al_2O_3$  bodies. Rasmussen<sup>(8)</sup> demonstrated that they exist in Verneuil grown sapphire and furthermore, that up to five zone refining passes are required before the sample becomes homogenized.

## 2. Consolidation

Considerable care was taken in die cleaning and powder transfer operations. All operations requiring exposed powder were conducted within a glove box. The precautions to prevent contamination have been described in detail previously.<sup>(7)</sup>

Table 2.3 lists the hot pressing conditions and results. All samples were 1-inch diameter by 3/16-inch thick. The fabrication cycle had been determined in the previous program. The only difference was that the time at temperature and pressure was reduced from 20 to 10 minutes. The purpose of the change was to reduce the grain size; however, no significant change was noted. The density of the fabricated samples all fell within the 99.6% to 99.9% dense range. The samples held for 20 minutes at temperature were all closer to the 99.8 - 100% dense range.

The samples that were machined into high temperature test specimens underwent extensive microstructural examination. Electron microscope techniques were used to measure the grain size on each test specimen. This, of course, gives a measure of the uniformity or lack of it within a hot pressed specimen. The average grain intercept for specimens from 1404 were  $0.80 \pm 0.05 \mu m$  indicating a uniform normal grain size distribution. Figure 2.1 illustrates a typical structure.



TABLE 2.2

SUMMARY OF EXPECTED HIGH PRESSED AND ANNEALED

HIGH PURITY ALUMINA IMPURITY CONCENTRATION

Impurity Element	As Pressed ppmw	Annealed ppmw
Li	0.3	0.3
B	3	1.5
C	160	10
N	3	1
F	10	5
Na	20	20
Mg	10	10
Si	15	15
P	1	1
Cl	40	15
K	10	10
Ca	10	10
Ti	1	1
Cr	1	1
Mn	1	1
Fe	2	2
Ni	5	5
Cu	0.5	0.5
Zn	1	1
Ga	1	1
S	<u>10</u>	<u>10</u>
Total	304.8	121.3

TABLE 2.3  
HIGH PURITY ALUMINA FABRICATION

Run Number	Temp. °C	Pressure Kpsi	Time min.	Density gm/cc	Grain Intercept microns
1352	1400	15	10	3.975	0.75
1358	1400	15	10	3.980	0.81
1368	1400	15	10	3.977	0.75
1404	1420	15	10	3.984	0.83
1410	1400	15	10	3.974	0.83
1417	1400	15	10	3.971	
1419	1400	15	10	3.980	
1420*	1400	15	10	3.969	

\* Linde A powder

### 3. Deformation Behavior

#### a. Analysis

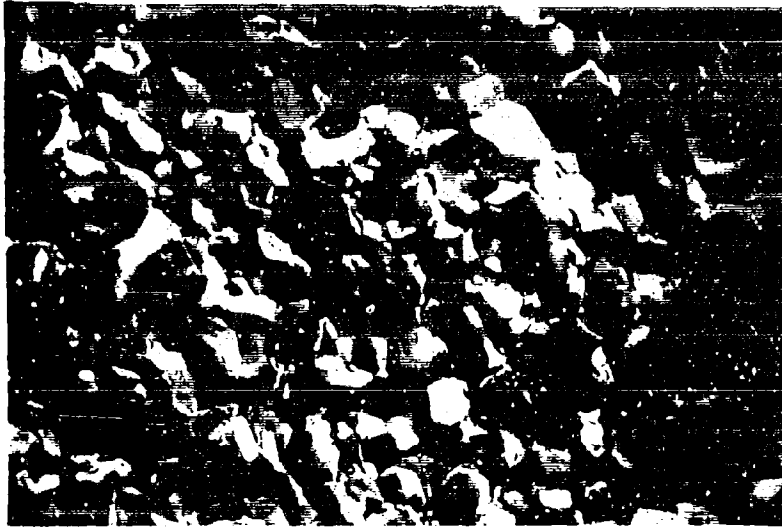
The analysis of the load-deflection data for plastic bending requires consideration beyond the elastic analysis. This results because the flow stress is, in general, a function of both strain and strain rate, and is not necessarily linear through the beam, thus invalidating the elastic stress analysis. When the stress is independent of strain and is linearly proportional to the strain rate, as in diffusional creep, the stress distribution is linear in the beam and the elastic equation may be used.<sup>(9)</sup>

A procedure has been developed for determining the stress-strain-strain rate relations for materials which strain harden and are rate sensitive.<sup>(10)</sup> This requires the measurement of the bending moment as a function of deflection and deflection rate and the determination of the outer fiber stress from the relation:

$$\sigma = \frac{M}{bh^2} [2 + m_b + m_b] \quad (4)$$

where  $m_b = \left( \frac{\partial \ln M}{\partial \ln \dot{\phi}} \right) \dot{\phi}$  (5)

$$m_b = \left( \frac{\ln M}{\ln \dot{\phi}} \right) \dot{\phi} \quad (6)$$



#691233

7500X

Figure 2.1 Ground Surface Showing Starting Microstructure of Test Specimen 1404-6 with Average Grain Intercept of 0.83 Microns.

where  $M$  is the bending moment,  $\phi$  the angle of inclination of the neutral axis of the beam (proportional to the deflection),  $\dot{\phi}$  the rate of change of  $\phi$ , and  $b$  and  $h$  are the width and depth of the beam. The strain and strain rate are determined directly from the deflection by geometrical considerations. During a test the load and the deflection are continuously recorded versus time and the "outer fiber" stress-strain, and strain rate are calculated from this data. In general, a series of constant rate bend tests are made from which the desired relations are calculated.

#### b. Test Results

A number of specimens were deformed at a constant strain rate through the test. Figure 2.2 is an example of a reconstructed (from the load and deflection versus time curves) moment,  $M$  versus strain rate curve where every attempt was made to maintain a constant  $\dot{\epsilon}$ . For convenience the approximate stress calculated from the elastic formula is also shown. This particular specimen was reversed after reaching the strain limits of the test fixture. During the reverse bending cycle the load was removed and the sample annealed for 5.45 minutes prior to reload for continuation of the test until fracture occurred at about 9% strain. There was a slight strain rate variation during the test as noted on Figure 2.2 for specific points of the test.

There are a number of interesting features of this test. Unlike most of the other deformation tests on  $Al_2O_3$  it was difficult to identify anything approaching a steady-state stress. However, most other studies stopped at 2-3% strain. Therefore, it was decided to identify any nearly level flow stress within 1-2% strain as the "steady state" stress. The point used for this test is designated in Figure 2.2. From 2-3% strain a small amount of strain hardening occurs. Upon reverse loading a pronounced Bauschinger effect is apparent in that the flow stress does not immediately reach the level at which it left off in the first cycle. Strain hardening continues at a rate about equivalent to that in the 2-3% strain range. After the mid-cycle anneal the specimen loaded very steeply to about 0.8 of the previous flow stress and exhibited what appears to be a yield phenomena. The slightly lower strain rate during this reloading was unfortunate, but assuming  $\sigma = K \dot{\epsilon}^{0.8}$  only a 500 psi change in flow stress would be noted. Thus, the 4000 psi lower flow stress appears to be a real result of the anneal. After nearly 1% of a fairly level flow stress a much steeper rate of strain hardening occurred until what appears to be non-catastrophic failure led to three stress minima prior to failure. Consideration was given to these minima being caused by a test related phenomena such as knife edge sliding, etc., but to date they have been observed under a variety of conditions. The interpretation of this curve will be given after the remaining mechanical and microstructural data is presented.

Figure 2.3 shows a second reverse bending experiment. This specimen was reversed twice to give a total strain of just over 12%. During the second cycle a problem in the recording of load was encountered so this data was not plotted, but the strain given the sample was taken into account. Both the temperature and strain rate were lower than the test plotted in Figure 2.2. The steady-state flow stress covers a larger strain interval and is somewhat flatter than the higher temperature test. The third cycle

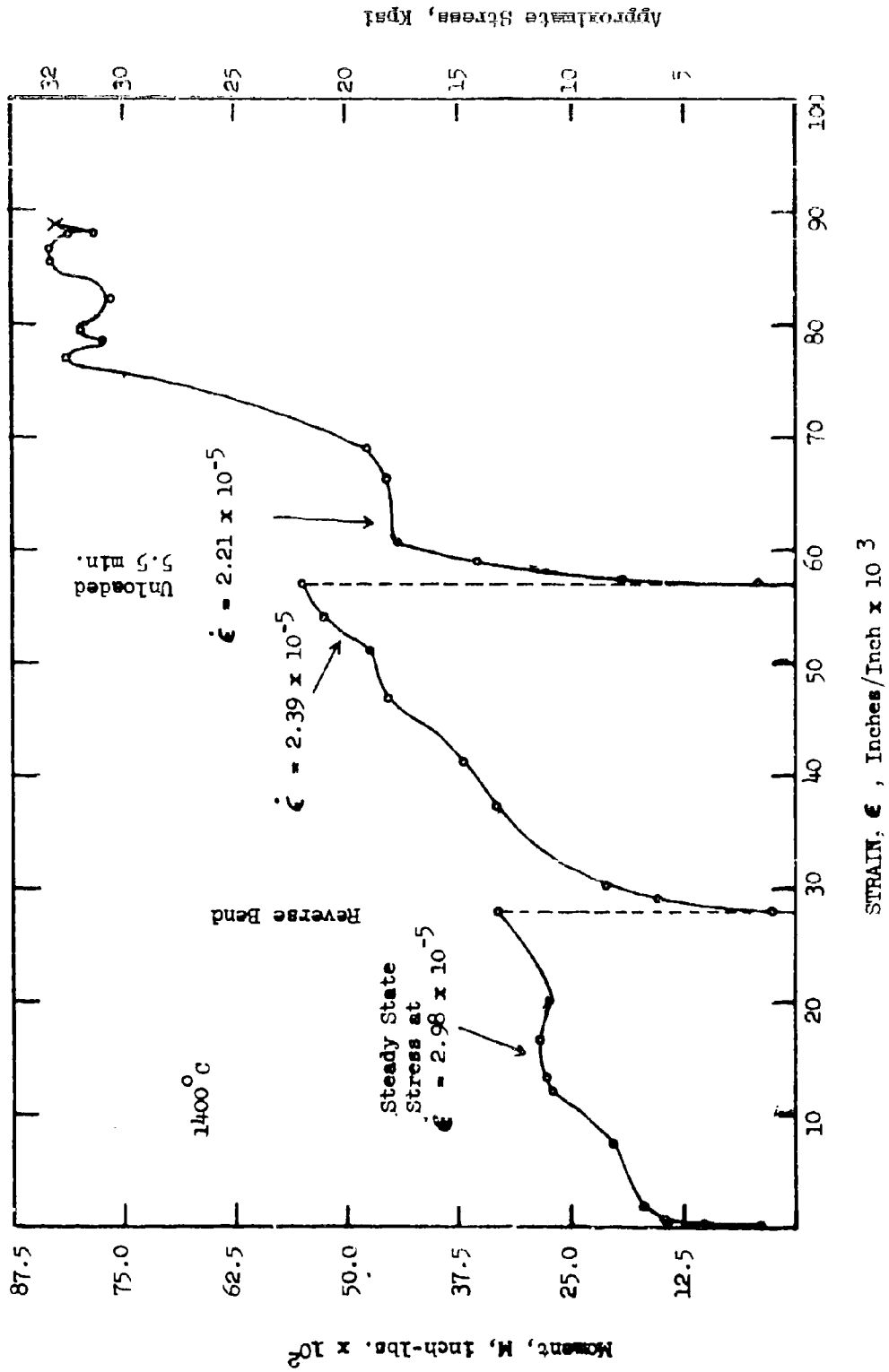


Figure 2.2 Moment and Stress versus Strain for High Purity Specimen 1404-4 with One Reverse Bending Cycle and 5.5 Minute Anneal in the Middle of the Reverse Bending Cycle.

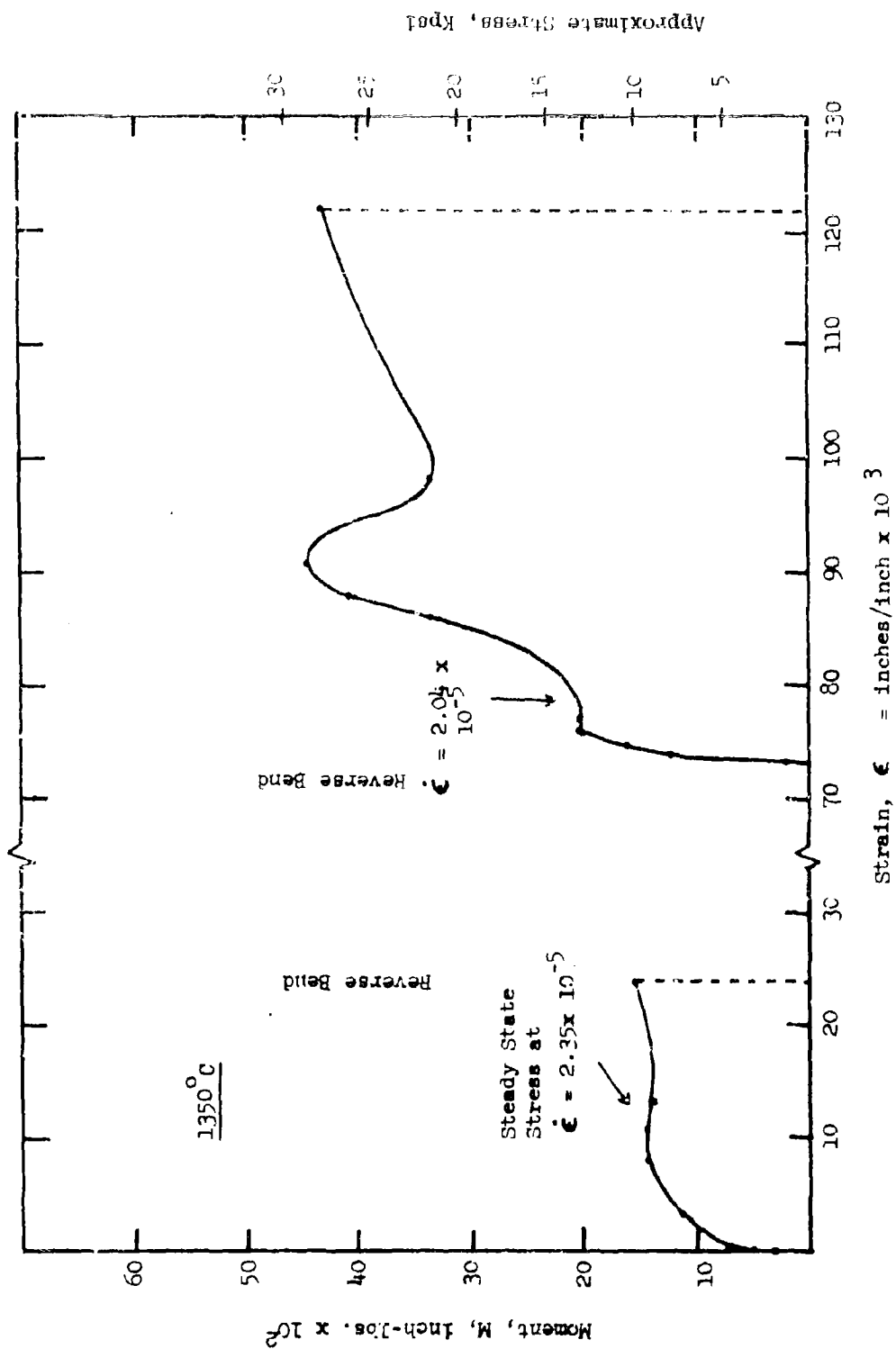


Figure 2.3 Moment and Stress versus Strain for High Purity Specimen 1358-3 with Two Reverse Bending Cycles. Load Recording Problems Prevented Plotting the Stress for the 1st Reverse Bending Cycle.

exhibits an apparent higher yield stress than the first cycle and what appears to be a slight yield stress drop. This is followed by a very steep strain hardening range. However, either a yield or microfailure mechanism caused a flow stress drop of about 5 Kpsi. Strain hardening again occurred up to the flow stress previously obtained. At this point the test was terminated due to the strain limitations of the test fixture.

Figure 2.4 illustrates a change of rate test conducted at 1400°C. Each plateau in the flow stress versus strain curve was obtained by successively raising the strain rate. The strain rate was not constant during the first 1% strain, but the flow stress at a specific strain and strain rate was identified and plotted in the flow stress versus strain rate curve (Figures 2.5 and 2.6). Strain rates were quite constant during the next three intervals of strain rate as were the flow stresses. The specimen fractured soon after the highest strain rate was imposed. The flow stress was nearly level so this point was also plotted.

The steady-state stress (using the elastic,  $\frac{3}{bh^2}$  stress calculation) from the first 2% strain was plotted versus strain rate in Figures 2.5 and 2.6 for tests at 1300, 1350 and 1400°C. Tests were conducted at 1450°C and 1480°C but flow stresses of about 30 Kpsi at  $\dot{\epsilon}$ s of  $4-5 \times 10^{-5}$  indicated that some mechanism, presumably grain growth, had hardened these specimens beyond the expected range for these temperatures (flow stress was roughly equivalent to the 1300°C tests). Electron microscopic examination showed that growth from 0.3  $\mu$ m to 3  $\mu$ m had occurred during the 1450°C tests. Thus, the lower temperature tests were chosen to compare with the lower purity, "standard" Al<sub>2</sub>O<sub>3</sub> + 1/4% MgO tests.

The scatter in the flow stress versus strain rate curves was much greater for the 1400°C data than the lower temperature tests. Because of the grain growth observed at 1450°C, grain growth was suspected as a contributing factor to the scatter. Tensile surface replicas from the individual test specimens failed to show the occurrence of significant grain growth. (Average grain intercepts of  $0.8 \pm 0.1 \mu$ m were obtained and these were within the scatter band of average grain intercepts of the starting material.) Fracture surface replicas revealed that some grain growth had occurred below the surface. The internal grain size was not determined for all of the samples, however.

Sample 1404-4-2 which was the sample tested in reverse bending had a post-test matrix exhibiting essentially a 1.50  $\mu$ m average grain intercept (Figure 2.7a). However, localized areas showed patches of 4 and 5  $\mu$ m grains (Figure 2.7b). The entire specimen cross-section was examined and these local areas of exaggerated growth were distributed throughout the section.

The time-temperature history above 1200°C was recorded for all but a few of the 1400°C test specimens. The area under the temperature-log time curve was integrated and recorded on Figure 2.6 in arbitrary units in parenthesis next to each data point to give a qualitative comparison of the thermal cycle each specimen received. It will be noted that the higher numbers correlate with data points farther from the best straight line while low numbers lie below the line. Thus, the argument that a small amount of grain growth prior to obtaining steady-state flow accounts for some of the scatter appears reasonable.

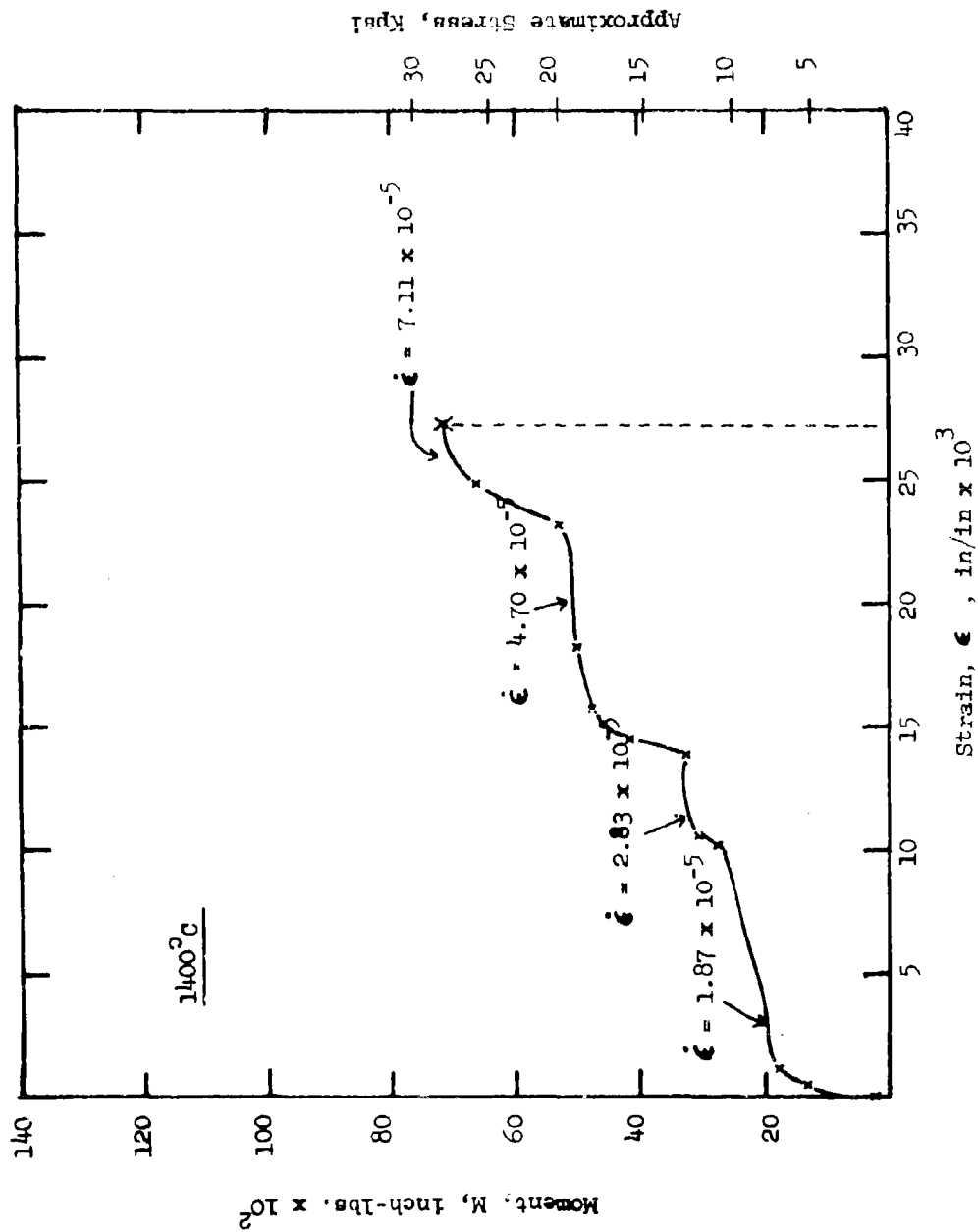


Figure 2.4 Moment and Stress versus Strain for Change of Strain Rate Test on Specimen 1404-6.



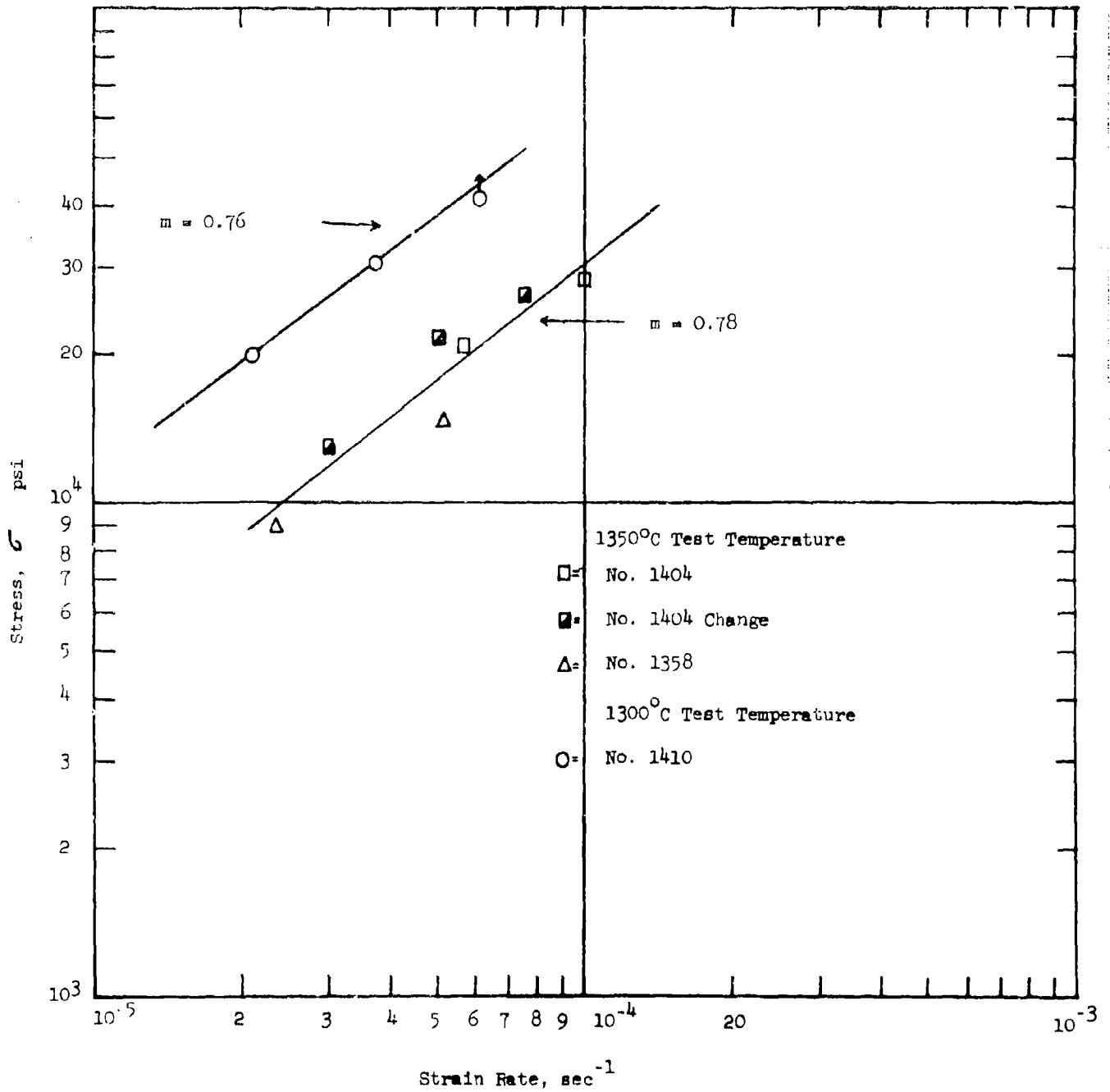


Figure 2.5 Steady-State Stress from First 2% Strain versus Strain Rate for High Purity  $\text{Al}_2\text{O}_3$  at 1300°C and 1350°C.

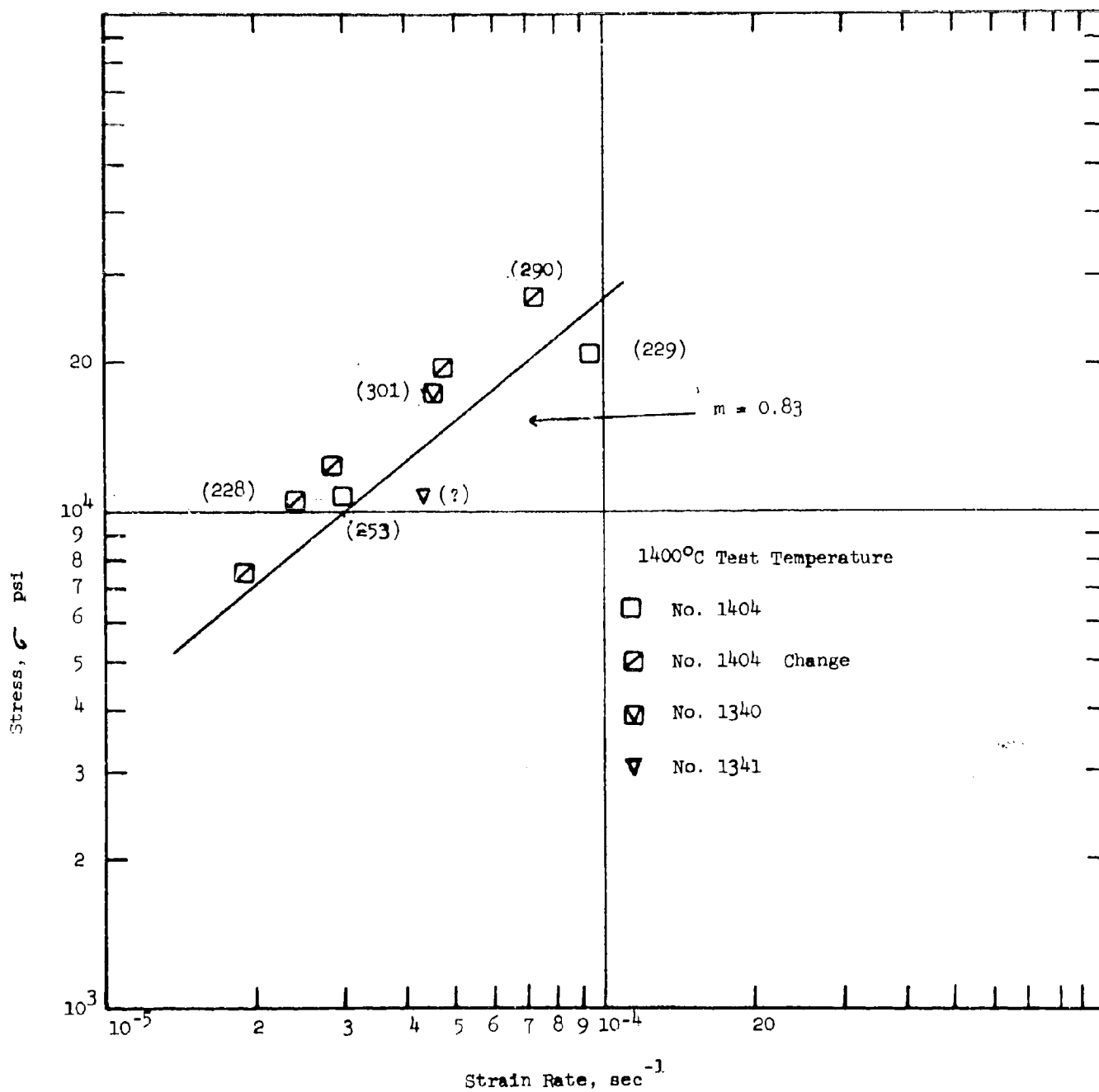


Figure 2.6 Steady-State Stress from First 2% Strain versus Strain Rate for High Purity  $\text{Al}_2\text{O}_3$  at 1400°C. Associated with each point is the integrated thermal cycle in degree-minutes above 1200°C for each specimen.



#691247

a

7500X



#691248

b

7500X

Figure 2.7 Fracture Surface of Specimen 1404-4 after Two Bending Cycles and 9% Strain at 1400°C, a) Showing Characteristic Structure of Major Portion of Cross-Section and b) Isolated Areas of Large Grains.

### c. Comparison of Two Alumina Bodies

The strain rate sensitivity,  $m$ , from Equation (1) is also noted on Figures 2.5 and 2.6 (between 0.76 and 0.83) for the high purity alumina (to be designated HP alumina). These are to be compared with  $m = 0.66$  at 1300°C and  $m = 0.61$  at 1400°C for 1.1  $\mu\text{m}$   $\text{Al}_2\text{O}_3 + 1/4\%$  MgO (to be designated standard alumina). An increase in  $m$  to 0.8 to 0.9 was noted in the standard alumina data with increased grain size to 5 to 10  $\mu\text{m}$ . This was previously interpreted as being due to an increased diffusional creep contribution compared with a competing grain boundary sliding mechanism at 1-3  $\mu\text{m}$  grain size. Thus, it is of considerable interest that such high values of  $m$  were obtained at sub-micron grain sizes.

The HP data is best compared with the standard alumina data by comparing the measured strain rate at a given flow stress. This is illustrated in Figure 2.8 at 10,000 psi. In the earlier work 5000 psi was the flow stress used in the extrapolations. However, in the temperature-strain rate range used for the present work there were no flow stresses measured this low so large extrapolations would be required. Thus, it was useful and perhaps more accurate to compare strain rates at a flow stress where actual data was gathered for both materials; 10,000 psi\*. The 1300°C and 1350°C points for the HP material were lower, but parallel with the standard  $\text{Al}_2\text{O}_3$  line. The 1400°C point fell badly off the line representing a significant reduction of strain rate or hardening. It has already been mentioned that grain growth was suspected as causing scatter in the 1400°C data. It is now further stated that grain growth probably caused the apparent hardening of the 1400°C data point in Figure 2.8. The assumption was made that this was the case and that grain growth from 0.8  $\mu\text{m}$  to 1.1  $\mu\text{m}$  (measured on one fracture surface for a one-cycle 1400°C test) occurred prior to the establishment of a steady-state flow stress. Further, it was assumed that  $\dot{\epsilon} \sim K \frac{1}{G^{2.5}}$  as found for standard alumina and an adjusted  $\dot{\epsilon}$  for

10,000 psi was found. This point is plotted in Figure 2.8 and it can be seen that the 1400°C data now fits an extrapolation of the lower temperature data. This, together with the observed growth, lends credibility to the assumption and calculation.

The effect of grain size can be factored into the comparison by plotting strain rate at a single temperature and flow stress versus grain size (Figure 2.9). The curve for standard alumina was taken from previous work (a different flow stress and temperature were used to reduce the chance of error in extrapolation). The lower creep rate for HP alumina stands out in this comparison with the HP alumina giving an effective creep rate of  $\sim 0.2$  the standard alumina at equivalent grain sizes.

The activation energies are indicated on Figure 2.8. The fact that HP  $\text{Al}_2\text{O}_3$  had a lower activation energy seemed to correlate with a trend

\* The  $\text{Al}_2\text{O}_3 + 1/4\%$  MgO flow stresses were calculated by the relation  $P_a = \frac{3Pa}{bh^2} (2 + m)$

whereas the present data was calculated from the elastic formula  $3Pa$ . To facilitate comparison to the  $\text{Al}_2\text{O}_3 + 1/4\%$  MgO data was increased  $bh^2$  to compare with the HP data. The correction involved about a 13% change in flow stress and simply rendered the comparison more accurate.

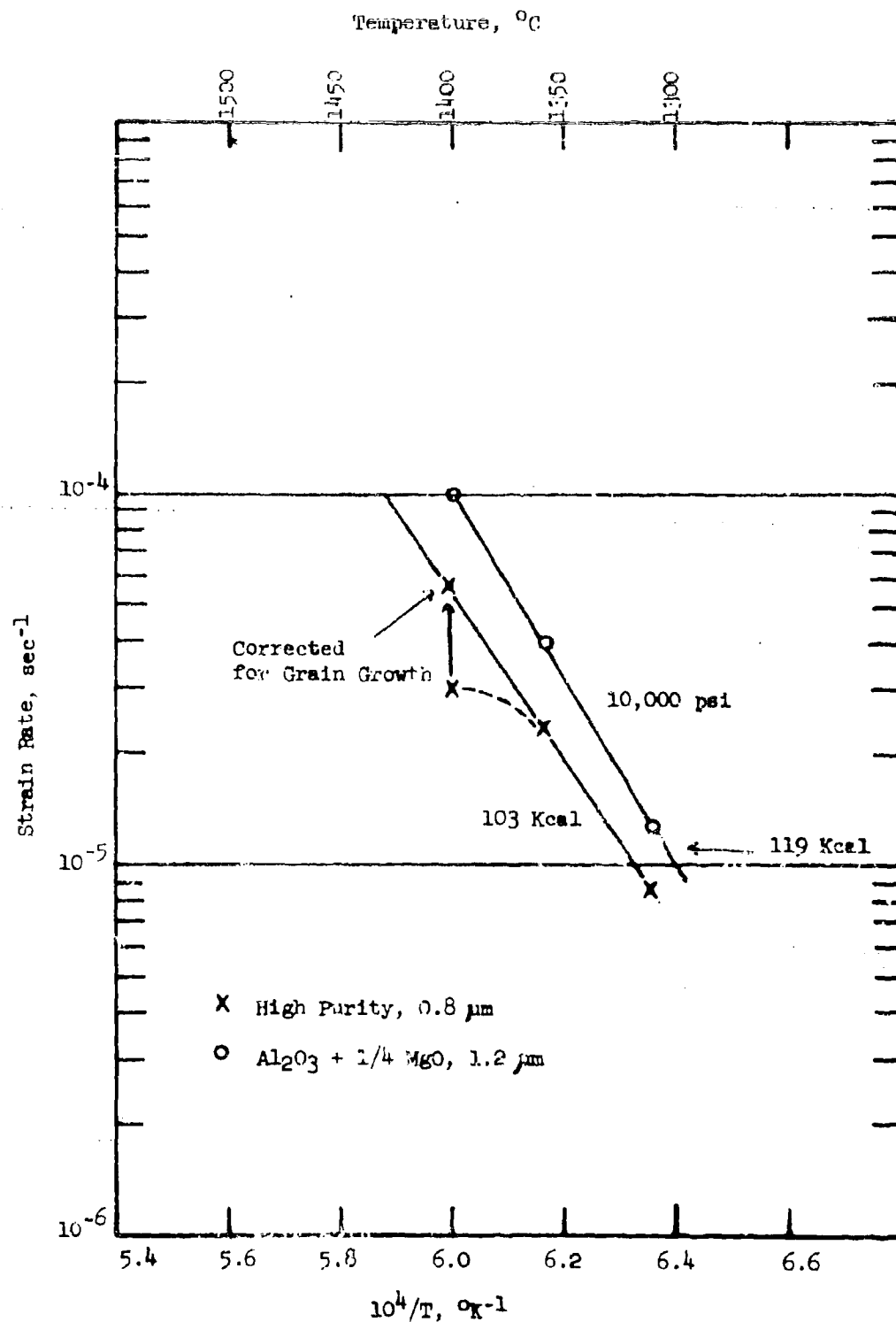


Figure 2.9 Strain Rate for 10 Kpsi Flow Stress for High Purity and Standard Alumina as a Function of Temperature.

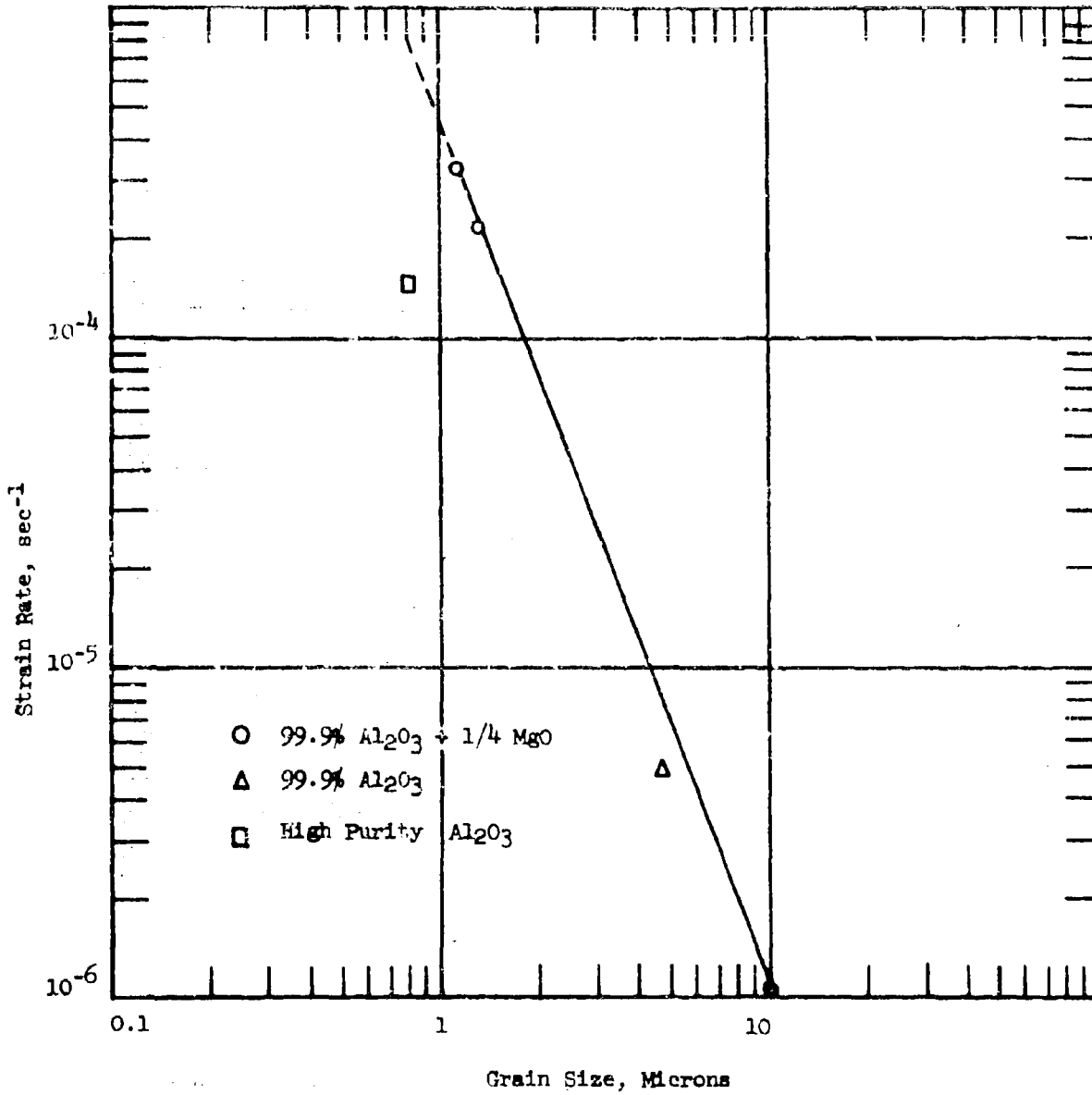


Figure 2.9 Strain Rate - Grain Size Relationship for Three Grades of Al<sub>2</sub>O<sub>3</sub>.

observed in the previous study.<sup>2</sup> Figure 2.10 shows the observed activation energies as a function of grain size. Also plotted are activation energies for 7, 15 and 34  $\mu\text{m}$  grain size Lucalox determined from the data of Folweiler,<sup>3</sup> at a stress of 5000 psi by the same technique as in Figure 2.8 (The 10  $\mu\text{m}$  Lucalox was measured by Heuer and Cannon.<sup>2</sup>) There is a general trend for increasing activation energy with increasing grain size. The data for the Coors  $\text{Al}_2\text{O}_3$  does not support the trend. There were many other features of the deformation behavior for this material that did not correlate with the other materials tested, thus it is not surprising that the activation energies fell off the line. Folweiler stated that the 7  $\mu\text{m}$  Lucalox underwent some grain growth during the testing. This growth would contribute the apparent low (with respect to the line) value of activation energy since there would be a larger grain size at each successive temperature.

The activation energy was plotted versus the temperature interval over which the data was gathered. It can be stated that there was sufficient overlap that the apparent activation energy is not a function of test temperature.

The  $\text{Al}_2\text{O}_3$  creep studies performed by others have been analyzed by the Nabarro-Herring creep equation (3). For comparative purposes, it was instructive to plot the HP alumina data on this curve (Figure 2.11) which also shows the lattice diffusion coefficients. The HP data were only slightly below the line representing the bulk of the data in the previous studies<sup>2</sup> and the data of Folweiler.<sup>3</sup> The actual data points lie below the standard alumina data as expected from the relation shown in Figure 2.9.

Because of the trend toward decreasing activation energy with decreasing grain size it was important to consider the Coble<sup>11</sup> treatment of the Nabarro-Herring model based on boundary diffusion:

$$\dot{\epsilon} = \frac{47.1 w D_b}{KT G^3} \quad (7)$$

where  $w$  is the boundary width and  $D_b$  the boundary diffusion coefficient.

The combined factor  $wD_b$  is shown in Figure 2.12 with creep data analyzed in an identical manner and  $wD_b$  factors from secondary grain growth studies by Mistler<sup>12</sup> initial sintering kinetics by Johnson and Berrin<sup>13</sup> and creep data of Chang.<sup>14</sup> The line for the HP  $\text{Al}_2\text{O}_3$  was quite distinct from the standard  $\text{Al}_2\text{O}_3$  which is probably a result of both increasing purity and the lower grain size.

#### d. Microstructure Study

As already mentioned extensive electron microscopy accompanied the deformation study. Figure 2.13 illustrates the surface structure of Sample 1404-4 and a control sample after the first and second cycle of bending. The stress-strain curve for this sample is shown in Figure 2.2. Figure 2.13 a and b illustrate the difference in the tensile and compressive surface after only 2.8% strain. The tensile surface (a) shows rounded grain surfaces and boundaries. There are regions (arrow) which show

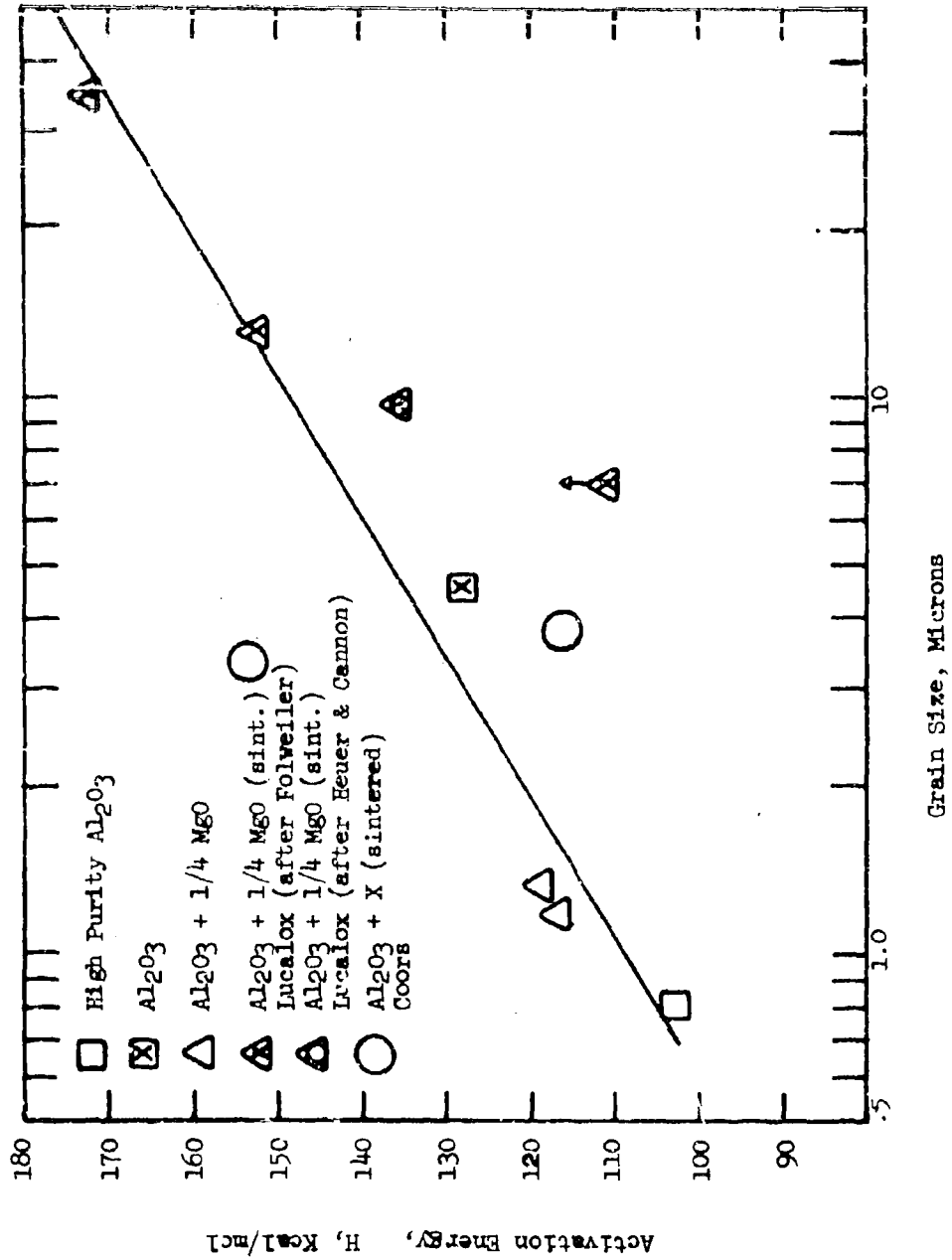


Figure 2.10 Activation Energy for Steady-State Creep as a Function of Grain Size for Several Materials.



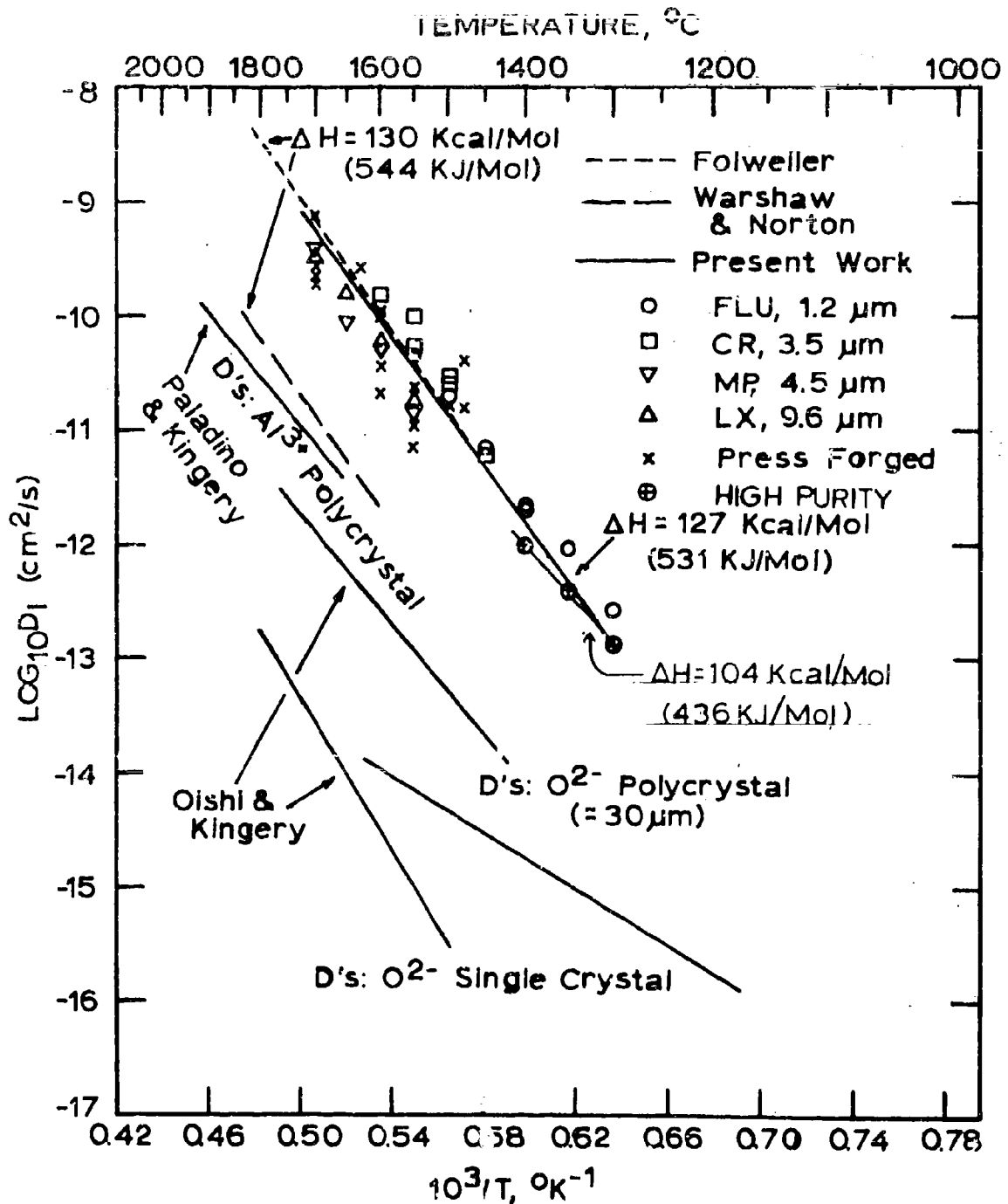


Figure 2.11 Diffusion Coefficients versus Reciprocal Temperature for Several Al<sub>2</sub>O<sub>3</sub> Bodies.

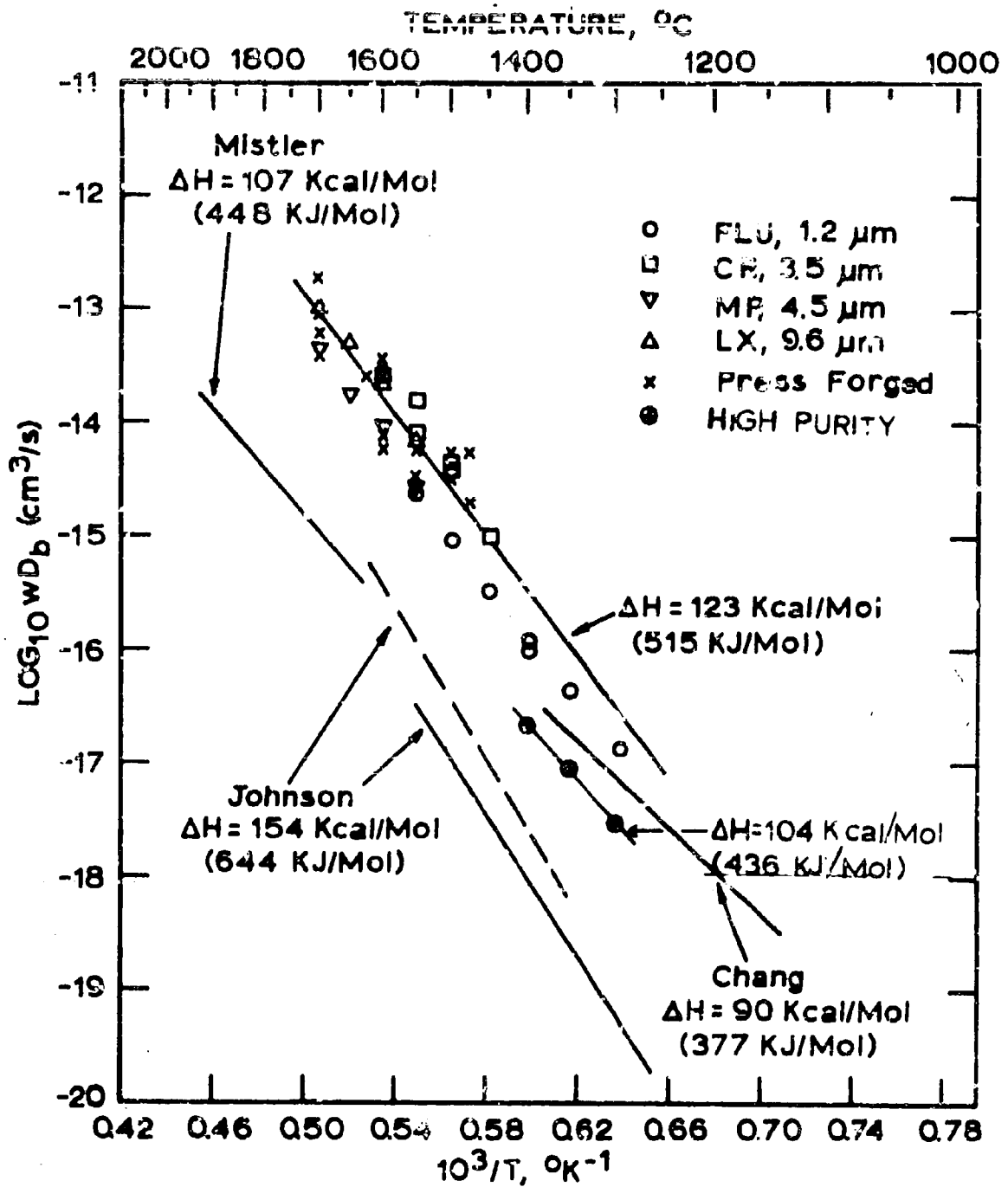


Figure 2.12 Product of Boundary Width Times Diffusion Coefficients versus Reciprocal Temperature.

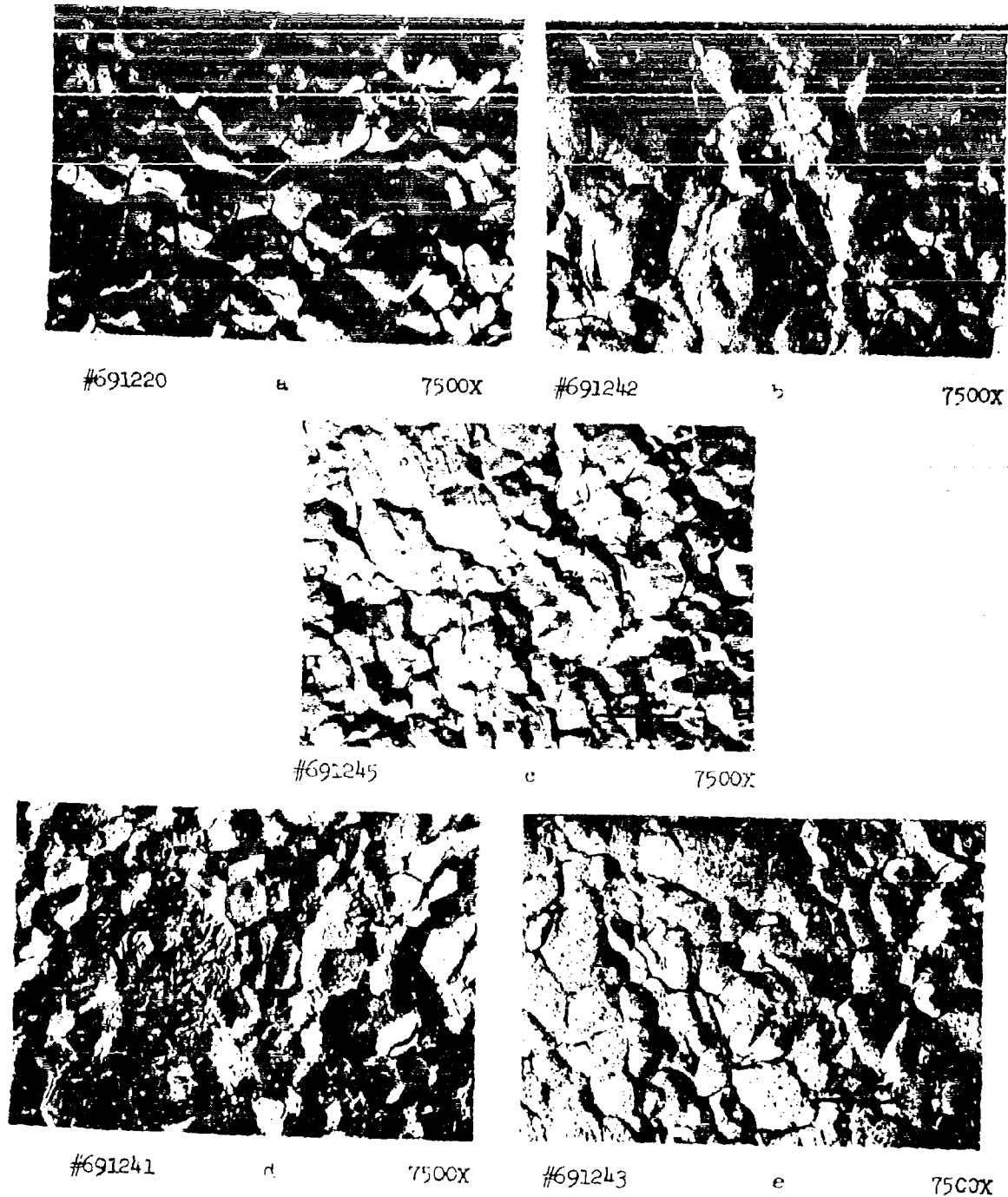


Figure 2.13 Surface Structure of Sample 1404-4 Tested at 1400°C;  
a) Tensile and b) Compression after 1st Cycle, c) Control  
Sample after 2nd Cycle, and d) Tensile and e) Compression  
after 2nd Cycle.

apparent double boundaries and many triple points having dihedral angles of  $4 \times 120^\circ$ . There are a few singularities of unknown origin on the surface. The most prominent feature of the compressive surface (b) is the high concentration of singularities. When these were noted early in the testing program a molybdenum sleeve was positioned between the testing cage and the furnace to prevent potential impurity vapors from entering the testing cell. This did not prevent the occurrence of the singularities proving that either the singularities were not of an impurity vapor origin or that the sleeve was not an effective barrier for the source (the ends of the sleeve were much colder than the hot zone, thus impurities coming from the hot zone of the furnace should have condensed). The grain boundaries of the compressive surface (b) look somewhat more angular and less regular than those of the tensile surface. A marked change in surface structure occurred during the second cycle of bending. The new compressive surface (e) which, of course, was the tensile surface (a) in the first cycle developed a structure quite similar, but perhaps somewhat more angular and disturbed than the original compressive surface (b). A high concentration of singularities developed and several heavily disturbed triple points (arrows) are apparent. The old compressive surface which became the tensile surface (d) during the second cycle developed a structure unlike any of the other three strained surfaces. A very angular within grain structure developed having as many as three principal orientations within any given grain. This structure is quite different from thermal etching which normally shows only two or perhaps a curved ledge development. Further, the grain boundaries are much less distinct than in the other surfaces and many of the features such as double boundaries and the unusual triple point structure already pointed out are apparent. The rounded singularities which were observed on this surface in the compressive mode are no longer apparent. This suggests that the singularities are not impurity phases but some etching phenomena that is free to develop under stress free or compressive surface stresses, but not tensile stresses. Point defect clusters, impurity centers on dislocations might react in this way. The control surface (c) shows a significant population of the singularities, some thermal etching and at least one area that looked like a double boundary (arrow) similar to the worked surfaces. In general, the boundaries were distinct and triple points regular with  $120^\circ$  angles.

High magnification examination of the strained surfaces revealed details of the features already mentioned plus several other phenomena. Figure 2.14 shows a good example of the wavy double boundary at position (A). This type of boundary is suggestive of extensive shear as typified by dislocation interactions with grain boundaries followed by the development of grain boundary dislocations. Another possibility is boundary migration with both the old and new boundary positions being thermally etched. The displaced triple point at (B) is suggestive of grain boundary sliding (GBS).

Figure 2.15 is a compressive surface and shows the apparent development or ghost of a  $0.25 \mu\text{m}$  grain structure within a  $2 \mu\text{m}$  grain. The structure could be caused by either polygonization after dislocation development or by the etching of a relic from the grains or powder during development. Figure 2.16 illustrates another example of sub-grains (A). In this case they appear to be associated with an irregular triple point, and



#691200

37,500X

Figure 2.14 Tensile Surface Structure of Sample 1404-1 Tested at 1350°C Showing Double Boundary (A) and Triple Point Offset (B).



#691173

37,500X

Figure 2.15 Compressive Surface of Sample 1358-2 after Second Cycle at 1350°C Showing what Appear to be 0.2% Micron Centos within a 2 Micron Grain.

strongly suggest that they result from polygonization resulting from the extensive shear associated with this deformed triple point. Also shown in this figure are several broad boundaries and what appears to be a triple point offset (B). This, of course, is an expected result of GBS.

The occurrence and disappearance of singularities as mentioned usually corresponded with stress-free or compressive surfaces. However, exceptions were found in this general view; and Figure 2.17 illustrates one example found on a tensile surface. Thus, it must be stated that the explanation of the singularities based on etching of a structural feature may be incorrect.

The other feature that has not been interpreted is the "within grain" lines shown in Figure 2.13 d. Many lines intersect at approximately a 60° angle. One possible interpretation is that they are slip traces. However, this is thought to be quite a radical explanation especially since the crystallography and known slip systems in alumina would focus on rhombohedral slip, a secondary slip system in alumina. The lines may be a result of thermal etching although the authors have not previously observed these features in thermally etched surfaces. It would appear that a conclusive explanation must await transmission electron microscopy of the surface grains.

#### e. Discussion of the Comparison Between Alumina Bodies

The decreased creep rate (at comparable temperature, flow stress and grain size) and increased rate constant for high purity alumina compared with moderate purity  $\text{Al}_2\text{O}_3 + 1/4\%$  MgO probably are interrelated. It is thought that non-Newtonian GBS is the principal cause of  $m < 1$ , the predicted value for diffusional creep. Recent work on  $\text{Al}_2\text{O}_3 + 1/4\%$  MgO suggests that dislocation motion may play a more significant role than previously thought in moderate temperature creep of alumina. Both microstructural and stress-strain evidence for dislocation multiplication, interaction and locking were obtained at high strains. This, of course, suggests that dislocation effects are an alternative explanation for the low  $m$  value in the fine-grained  $\text{Al}_2\text{O}_3 + 1/4\%$  MgO. It is also thought that there is a diffusional component to creep. In fact, diffusional creep requires some GBS to allow the process to continue. Conversely, if GBS is the dominant mechanism, some diffusional creep or alternatively shear are required to relieve back stresses at triple point intersection etc., and allow homogeneous flow.

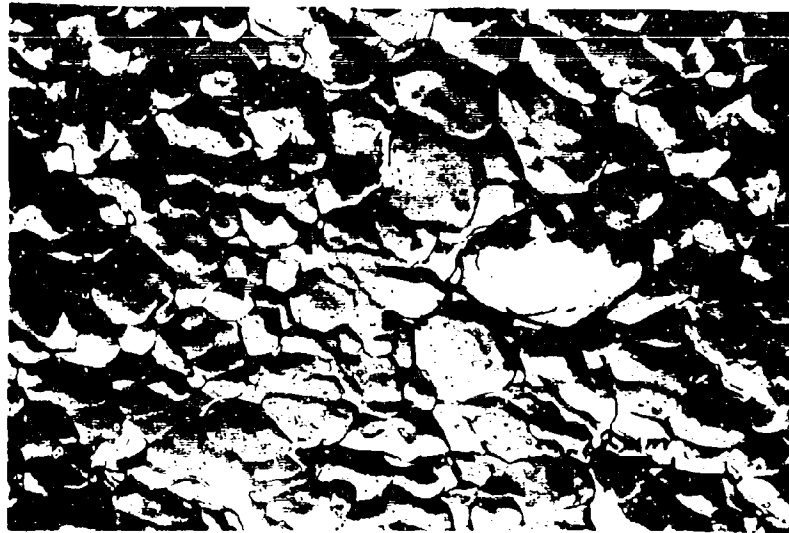
Thus, the distinctive effects on creep by the alteration of chemistry probably result from a decreased importance of non-Newtonian GBS in HP alumina. It is reasonable to predict that a marked reduction of impurities or  $\text{Mg}^{+2}$  in the grain boundary "region" would markedly reduce the ease of GBS. This would shift the competing (or complementary) mechanism of creep toward the diffusional creep side giving the observed higher  $m$  value. One alternative explanation based on a dislocation model for creep involves the ease of dislocation multiplication or generation at grain boundary ledges. The high boundary mobility in HP alumina would absorb dislocation sources giving the observed increase in  $m$  value. Again, this would shift the controlling mechanism toward diffusional creep. Arguments could be advanced considering a shift from extrinsic to intrinsic diffusional creep control with increasing purity and resulting in decreased creep rates, but these are not required to



#691128

22,500X

Figure 2.16 Tensile Surface of Sample 1358-1 Tested at  $1450^{\circ}\text{C}$  Showing Apparent Polygonization Associated with Triple Point Irregularity (A) and Triple Point Offset (B).



#691237

7500X

Figure 2.17 Tensile Surface of Sample 1404-6 Tested at  $1400^{\circ}\text{C}$  Showing One of Few Examples of Singularities on Tensile Surface.

fit the data (although it is possible that intrinsic diffusion is operative). The simple fact that creep rates are reduced together with an increase in  $m$  suggests that diffusional creep *per se* is a slower process, and by eliminating the ease of GBS, or dislocation multiplication, diffusional creep becomes the dominant mechanism.

These findings are in conflict with those of Hewson and Kingery<sup>11</sup> who found a constant creep rate for increasing  $Mg^{+2}$  from 1 to 20 ppm and then a decreasing creep rate with increasing concentration from 20 to 2500 ppm. They interpreted their results as diffusional creep and explained the effect of  $Mg^{+2}$  on the basis of its effect on the diffusion rate. Their material was  $> 10 \mu m$  grain size so that higher  $m$  values would be expected to be obtained (the previous studies by Heuer and Cannon found increasing  $m$  values above  $5 \mu m$  grain size). Thus, by altering  $Mg^{+2}$  concentration at large grain sizes they were apparently affecting diffusion rates whereas by varying  $Mg^{+2}$  and other ions at small grain sizes, we were apparently causing a shift in controlling mechanism from GBS to diffusion.

The lower activation energy with decreasing grain size probably is caused by the increased importance of grain boundary diffusion control. In most systems, where grain boundary diffusion rates have been measured, the activation energy is lower for grain boundary diffusion than lattice diffusion. Also, the  $\dot{\epsilon} \sim G^{-2.5}$  dependence is midway between that predicted for lattice diffusion controlled creep  $\dot{\epsilon} \sim G^{-2}$  and boundary diffusion controlled creep  $\dot{\epsilon} \sim G^{-3}$ . The HP  $Al_2O_3$  grain boundary diffusion curve fell below the standard and larger grain  $Al_2O_3$  and also agreed quite nicely with the line by Chang for creep and Mistler for secondary grain growth. These four facts combined with the marked increase in grain boundary area with decreasing grain size led to the assertion that the cause of the observed relations is a shift toward grain boundary diffusion control.

This explanation does not specifically mean that a grain boundary diffusional creep model is invoked for both grades of fine grain  $Al_2O_3$ . Deformation mechanisms such as GBS or dislocation motion certainly require diffusion for accommodation, perhaps diffusion around a ledge, or climb. Thus, the decreasing activation energy with decreasing grain size is thought simply to be caused by the ever increasing importance of grain boundary diffusion for any one of the three major deformation processes. It generally would be expected that dislocation mechanisms such as climb over obstacles would be controlled by lattice rather than boundary diffusion; however, the indications of dislocation activity seen to date are intimately related to the behavior of the grain boundaries and so should also reflect such a change in the diffusion process. Therefore, it is concluded that the affect of increased purity at these fine grain sizes has been to shift the controlling mechanism somewhat away from non-Newtonian GBS toward diffusional creep.

#### f. Discussion of Deformation at High Strains

At strains above 2%, strain hardening to flow stress as much as 3 times the "steady state stress" occurred. Grain growth during test is one possible cause of apparent strain hardening. In fact, calculations of predicted flow stresses for the observed grain growth in Sample 1404-4



(Figure 2.2) indicated that virtually all of the strain hardening could be accounted for by this mechanism. However, it is thought that this mechanism is too simple in view of the complicated shape of the stress-strain curve and microstructural evidence for structural alterations as a result of strain.

The Bauschinger effect (Figure 2.2) is typically explained as being a result of easy dislocation flow in the reverse direction of that experienced in a previous cycle where dislocation impingement on a barrier such as a grain boundary caused hardening. Such behavior can be partially rationalized in terms of relief of stresses at triple points and other obstacles to sliding. This is thought to be the cause of the anelastic recovery which has been observed after creep of BeO and  $Al_2O_3$ <sup>14</sup>. However, grain growth would not give rise to this effect.

After the anneal in the middle of the second cycle in test 1404-4 (Figure 2.2) a rather sharp apparent yield stress was observed. Also, the flow stress was lower than that observed just prior to the anneal. If grain growth was the cause of the hardening the lower flow stress would not have been observed. However, polygonization or partial annihilation of dislocation structures at grain boundaries would have softened the material. It would also have allowed the observed period of steady-state stress prior to the resumption of strain hardening. A similar sharp yield point was observed in the test illustrated in Figure 2.3 with a short interval of easy flow prior to a very steep rate of strain hardening.

The microstructural evidence for wavy and double grain boundaries together with evidence for polygonization also support the view that dislocation flow, locking, multiplication and polygonization are influential in the extended strain region of fine-grained  $Al_2O_3$  deformation.

Microstructural evidence for grain boundary sliding was also evident, thus the role of GBS in the high strain regime must be considered. GBS could be the major deformation mechanism requiring diffusion or dislocation flow for strain accommodation, or GBS could be the secondary process required by the other processes as already mentioned. But, consider the possibility that GBS is the major deformation mechanism. The Bauschinger effect noted in Figure 2.2 could be explained by a reversal of GBS as well as by a dislocation model. Thus, it is not possible at this time to determine the relative contributions of the three principal deformation mechanisms, but this work supports the view that diffusion, sliding and dislocation flow all play a role in the deformation of  $Al_2O_3$  to high strains in the 1300-1450°C range.

The failure of  $Al_2O_3$  in the moderate temperature range apparently is less catastrophic than previously thought. The occurrence of three flow stress reductions prior to failure in Figure 2.2 is a dramatic demonstration of this accommodation. A related study<sup>5</sup> on standard alumina resulted in the development of a crack covering 1/10 of the bar width on the second bending in a rebend test. This crack closed on the third bend as the surface was in compression. But, on the fourth bend, the crack opened to cover 1/4 of the bar width, the flow stress was 15 Kpsi and the bar remained unbroken at the end of the test. Since the flow mechanism at high strains still remain unclear it follows that failure and crack accommodation are less understood.

#### 4. Fracture Strength

The fracture strengths of the high purity alumina are compared with the data of Spriggs, Mitchell and Vasilos<sup>15</sup> on 99.9%  $\text{Al}_2\text{O}_3$  at two grain sizes in Figure 2.18. Also shown in this graph are some test data for 1.1  $\mu\text{m}$  grain size  $\text{Al}_2\text{O}_3 + 1/4\%$   $\text{MgO}$ . The high temperature test data was collected during creep studies, so a variety of strain rates were involved and no attempt was made to factor this into the comparison except that the data of Spriggs et al was taken at  $10^{-4} \text{ sec}^{-1}$  whereas the new data was taken in the range  $2-9 \times 10^{-5} \text{ sec}^{-1}$ .

The fracture strengths demonstrate that the HP alumina strength is slightly stronger than 1-2  $\mu\text{m}$  grain 99.9  $\text{Al}_2\text{O}_3$  at the uppermost temperatures. Also, the strength at 1450°C appears to exceed that for  $\text{Al}_2\text{O}_3 + 1/4\%$   $\text{MgO}$ . The suppression of GBS or dislocation flow for HP alumina already discussed in comparing creep rates could also be responsible for the higher strengths. The high boundary mobility and small amount of grain growth at 1450°C may result in a further rise in the 1450°C data due to the strong effect of grain size on flow stress.

#### D. Summary

1. Uniform 0.8  $\mu\text{m}$  grain intercept 99.8% dense  $\text{Al}_2\text{O}_3$  specimens with an annealed 300 ppm total and 80 ppm cation impurities were fabricated.
2. Impurities are inhomogeneously distributed in both the powder and fabricated specimens.
3. A comparison of "steady-state stress" within the first 2% strain normalized for grain size for high purity  $\text{Al}_2\text{O}_3$  and  $\text{Al}_2\text{O}_3 + 1/4\%$   $\text{MgO}$  revealed that the HP  $\text{Al}_2\text{O}_3$  had approximately a factor of five (5) lower creep rate, a higher strain rate sensitivity, a lower activation energy, and grain boundary diffusion coefficients in agreement with several literature values. It is probable that this is due to an increased dominance of boundary diffusional creep over either grain boundary sliding or dislocation flow. Grain boundary sliding is the most likely process to be influenced by increased purity in this manner.
4. At high strains evidence was obtained for strain hardening, a Bauschinger effect and a sharp yield point upon reloading after a short mid-cycle anneal. Microstructural evidence supported the view that dislocation interaction and grain boundary sliding contributed to the high strain effects. Some of the strain hardening was probably due to grain growth during the test.
5. The occurrence of several stress maxima and minima prior to failure indicates that  $\text{Al}_2\text{O}_3$  has an apparent capacity for blunting a would-be catastrophic failure event.

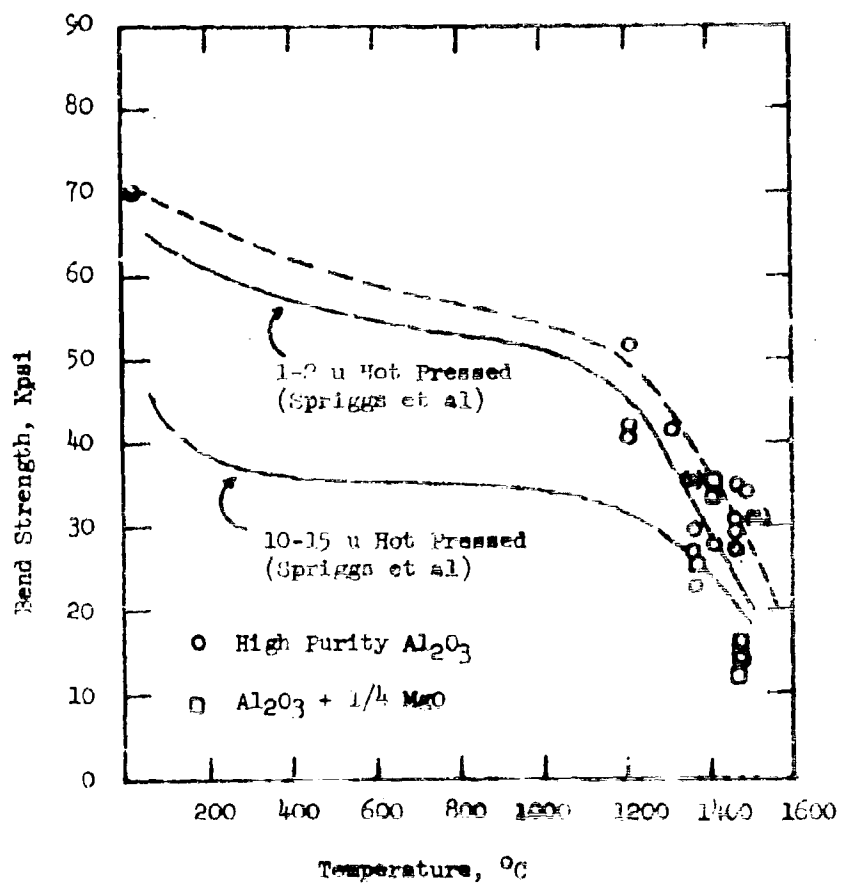


Figure 2.18 Bend Strength as a Function of Temperature for Several Grades of Alumina.

6. The increased high temperature strength for high purity  $Al_2O_3$  was probably due to the suppression of grain boundary shear initiated failure resulting from a lower concentration of segregated boundary impurities.

### III. HEAT FORGING ALUMINA

#### A. General

Studies over the last several years have been concerned with the hot working of  $Al_2O_3$  and MgO. Emphasis has been placed on  $Al_2O_3$  since the studies have revealed considerable new technology. Alumina single crystals were grown by the strain anneal technique<sup>16</sup> and alumina with high in-line transmission was produced.<sup>17</sup>

The subsequent work<sup>6,7,18,19</sup> revealed that deformation-recrystallization processes usually associated with metal working practice were responsible for the structures and properties observed. The deformation process itself produced a highly elongated grain structure with the long axis of the grains normal to the pressing direction. Upon primary recrystallization the microstructural texture was often destroyed, but a crystallographic texture which had accompanied the grain texture was retained. Also accompanying primary recrystallization and the equiaxed microstructure resulting from the process was a pore removal mechanism. It was suggested<sup>18</sup> that the porosity distributed throughout the structure presented preferred nucleation sites for the new generation of grains. This process itself could absorb porosity or the structure could be more susceptible to continued densification due to the nearness of pores to grain boundaries; their potential sink. Many details concerning the deformation-recrystallization remain unanswered; e.g., what role does strain induced grain growth play and is true grain refinement possible, what is the minimum temperature for recrystallization and what secondary deformation processes allow the homogeneous deformation of a billet, etc?

There are at least three potential motivations for forging  $Al_2O_3$ . They are, 1) the production of complicated shapes where a fine-grained dense microstructure is required, 2) improved mechanical properties due to the texture and retardation of structure sensitive failure mechanisms, and 3) high in-line optical transmission due to the crystallographic texture and the elimination of light scattering from birefringence. The mechanical properties have been studied extensively,<sup>6</sup> and it was found that the strength at  $-196^\circ C$  and  $1200^\circ C$  was nearly independent of grain size in the 1-20 micron range. However, there was no apparent effect of texture on the mechanical properties between  $1475-1700^\circ C$ , the plastic range.<sup>7</sup> In view of the results in Section II where definite indications of non-diffusive deformation processes after a few percent strain were presented the above finding should be reconsidered.

Some very interesting shape forging were accomplished; namely,  $60^\circ$  cones and a near hemisphere were produced. Lack of explicit knowledge of the flow and failure criteria for the temperature interval ( $1800-1950^\circ C$ ) in which most of the forging is conducted prevented further major gains in shape forging. Improved in-line transmission has been the most dramatic outcome of the forging effort.<sup>17</sup> In-line light transmissions of 60% were achieved for the forged material as compared with a maximum of 20% for the

best randomly oriented pore-free  $Al_2O_3$  available at an equivalent thickness. The main limitations of the process were the extent of the transparent zone, complete pore removal and the extent of the crystallographic texture.

The work to be described in the following section was aimed toward increased understanding of the hot working process, the production of fully dense alumina and mechanical property studies of high density textured alumina.

#### B. Material and Procedure

The forgings were conducted with 99.9+% pure  $Al_2O_3$  from three sources:

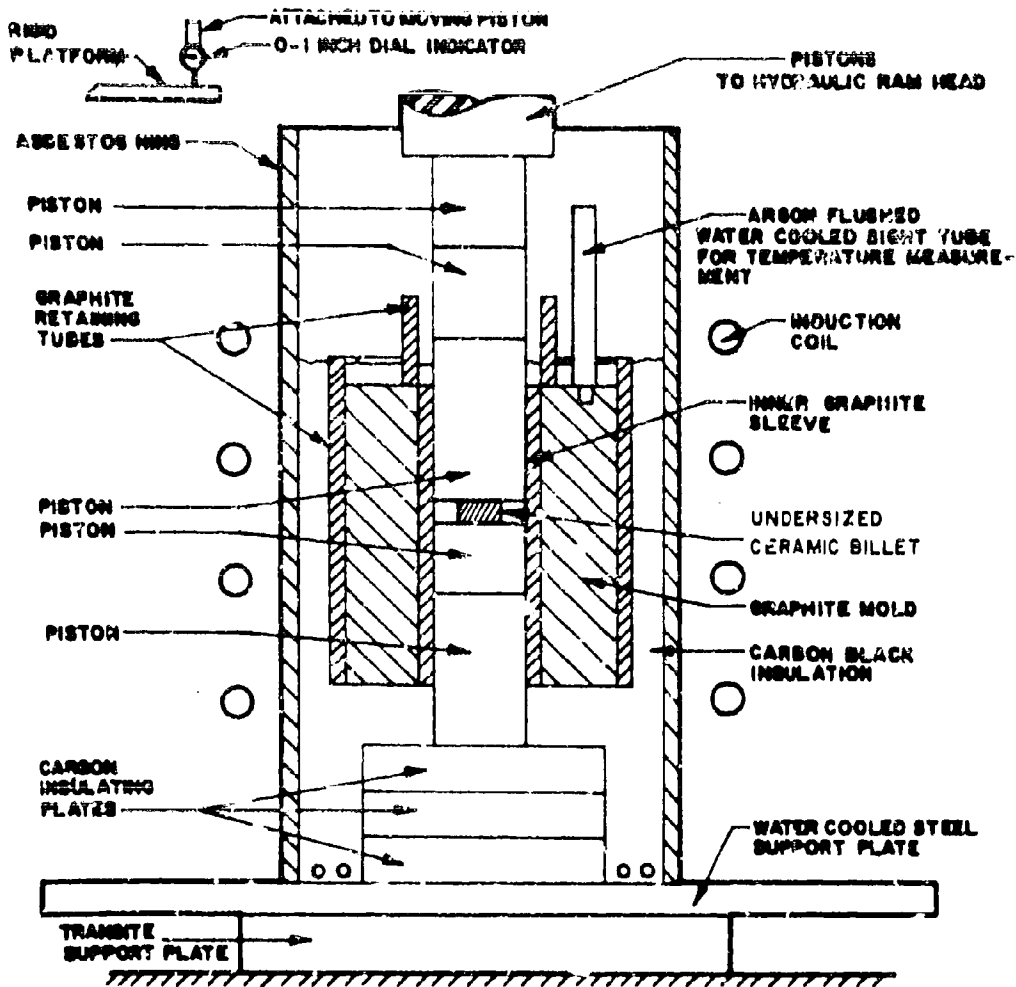
1. Code M-1, A. Meller Co., Providence, R.I., 0.3 micron  $Al_2O_3$ , mainly alpha but containing 10-20% gamma  $Al_2O_3$ ,
2. Code G-1,2, experimental powder from W.R. Grace Co., Clarksville, Md., 0.2 micron alpha  $Al_2O_3$  containing 0.1%  $MgO$ ,
3. Code L-1, Linde A from Union Carbide Co., Chicago, Ill., 0.3 micron  $Al_2O_3$ , similar phases to M-1. The only forging on this powder was with a hot pressed billet C-31 having a 1-2 micron grain intercept and 99+% density.

The forgings were conducted in a conventional induction heated graphite hot pressing furnace and press (Figure 3.1). CS graphite was used for the mold sleeves while the pistons and mold were made from ATJ graphite. The starting powder or billet conditions were arranged such that lateral flow was unrestricted during the deformation step. This was accomplished by either, 1) cold pressing the powder at 4 Kpsi in the graphite die and allowing unrestricted normal densification and shrinkage to occur during the heat up and dwell period prior to forging, or 2) forging and undersized sintered or hot pressed billet (34-99% dense) or preforged (~99% dense) billet. All forgings were conducted in an ambient atmosphere present within the essentially graphite systems. At 1860°C the atmosphere is expected to be C, CO,  $CO_2$  with CO the major species. The die lubrication-separating media system was constant throughout as this question had been the subject of a previous effort.<sup>6</sup> The graphite pistons were faced with molybdenum foil onto which boron nitride powder was sprayed.

Four-point bend tests were conducted in argon from 25 to 1500°C on 0.050 x 0.125 x 0.875 specimens. The 25°C tests were conducted by first heating the specimens to 900°C for a 1-hour hold, then cooling to 25°C and testing without breaking the argon atmosphere. The purpose of the anneal was to desorb any potential corrosive species and complete the test without re-adsorption. This potentially gives a measure of the intrinsic 25°C strength.

#### C. Results and Discussion

The forging conditions are listed in Table 3.1. The first five forgings were aimed toward achieving theoretical density along with a strong



65-8218

Figure 3.1 PRESSURE SINTERING APPARATUS USED FOR PRESS-FORGING EXPERIMENTS. NOTE THAT PRIOR TO FORGING, THERE IS NO CONTACT BETWEEN THE SPECIMEN AND THE DIE BODY

TABLE 3.1

Al<sub>2</sub>O<sub>3</sub> FORGINGS

Billet No.	Powder Type	Separating Media	Forging Temp. °C	Heating Time min.	Final Pressure psi	Time to Bring to Final Pressure	Time to Zero Strain	Total Time at Temp. and Pressure
1189	M-1-Al <sub>2</sub> O <sub>3</sub>	Mo-BN	1850	110	5600	10	55	70
1191	M-1-Al <sub>2</sub> O <sub>3</sub>	Mo-BN	1850	120	5600	10	25	70
1204	1189	Mo-BN	1880	60	5000	15	30	240
1222	M1-pre-sintered to 35% dense	Mo-BN	1860	70	5000	6	97	127
1232	M1-pre-sintered to 85% dense	Mo-BN	1860	75	5000	10	65	80
1240	Grace Lot 2156-AM7	Mo-BN	1740	45	5000	7	25	47
1277	Grace Lot 2156-AM8	Mo-BN	1850	65	5000	10	35	35
1282	Grace Lot 2156-AM8	Mo-BN	1650	60	5000	9	25	60
1294	L-1 hot pressed 99+ dense	Mo-BN	1750	60	yield 3400 psi	1 1/2	stopped at 64% height reduction	2 1/2
1297	A-AM8	Mo-BN	1750	59	5000	8	35	35

crystallographic texture. The remaining forgings with the exception of 1294 were conducted to study the influence of forging temperature on recrystallized grain size and degree of crystallographic texture. A second goal was to be able to produce a uniform (within the billet) high density microstructure which would be suitable for further mechanical property studies. Forging 1294 was the only forging conducted on a dense billet in this period. The object of this experiment was to forge quickly and then hot eject the billet to quench in the microstructure representative of the early stages of recrystallization.

### 1. Crystallographic Texture

In a hot working study it is a necessity to have some technique for determining preferred orientation and degree of texture. This is best accomplished by x-ray diffraction techniques. A technique was described<sup>6</sup> which is not as tedious as the construction of a pole figure, but which allows the evaluation of relative degrees of orientation. This system will be reviewed and illustrated by presentation of the x-ray data for sintered\* specimens, hot pressed billets of two length: diameter ratios and press forged Al<sub>2</sub>O<sub>3</sub>.

The diffraction pattern of a random (powder) sample was obtained. Values of  $f_0(h,k,l)$  defined by the relation

$$f_0(h,k,l) = \frac{I(h,k,l)}{\sum_{hkl} I(hkl)}$$

were calculated.

Similarly, values  $f(hkl)$  were calculated from the diffraction pattern of a forged specimen. The ratios  $R(hkl) = \frac{f(hkl)}{f_0(hkl)}$  which give the relative intensity of reflection were calculated against the angle  $\phi$  between the planes (hkl) and the basal plane.

In the case of a random (powder) sample,  $R$  has the constant value of unity. In the case of a perfectly oriented sample,  $R$  is zero everywhere except at  $\phi = 0$  where it has some large finite value. In the case of a distribution of orientation, in general,  $R$  will decrease monotonically from  $\phi = 0$  to  $\phi = 90^\circ$ . The better the crystallites are aligned, the higher the intercept at  $\phi = 0$  and the steeper the drop with increasing  $\phi$ .

Measurements of  $R$  as a function of  $\phi$  for Al<sub>2</sub>O<sub>3</sub> prepared in three ways are shown in Figure 3.2. Typical results for forged Al<sub>2</sub>O<sub>3</sub> are shown while specific results will be presented in subsequent paragraphs. The forged material usually exhibits the strong increase in  $R$  value at low  $\phi$  indicating a preferred basal orientation; the (0001) plane normal to the pressing direction. The two hot pressed samples illustrate some rather interesting results. In both cases pressure was applied to the sample at some low temperature ( $\sim 700^\circ\text{C}$ ) and kept constant throughout the remainder of

\* Lucalox purchased from General Electric Co.



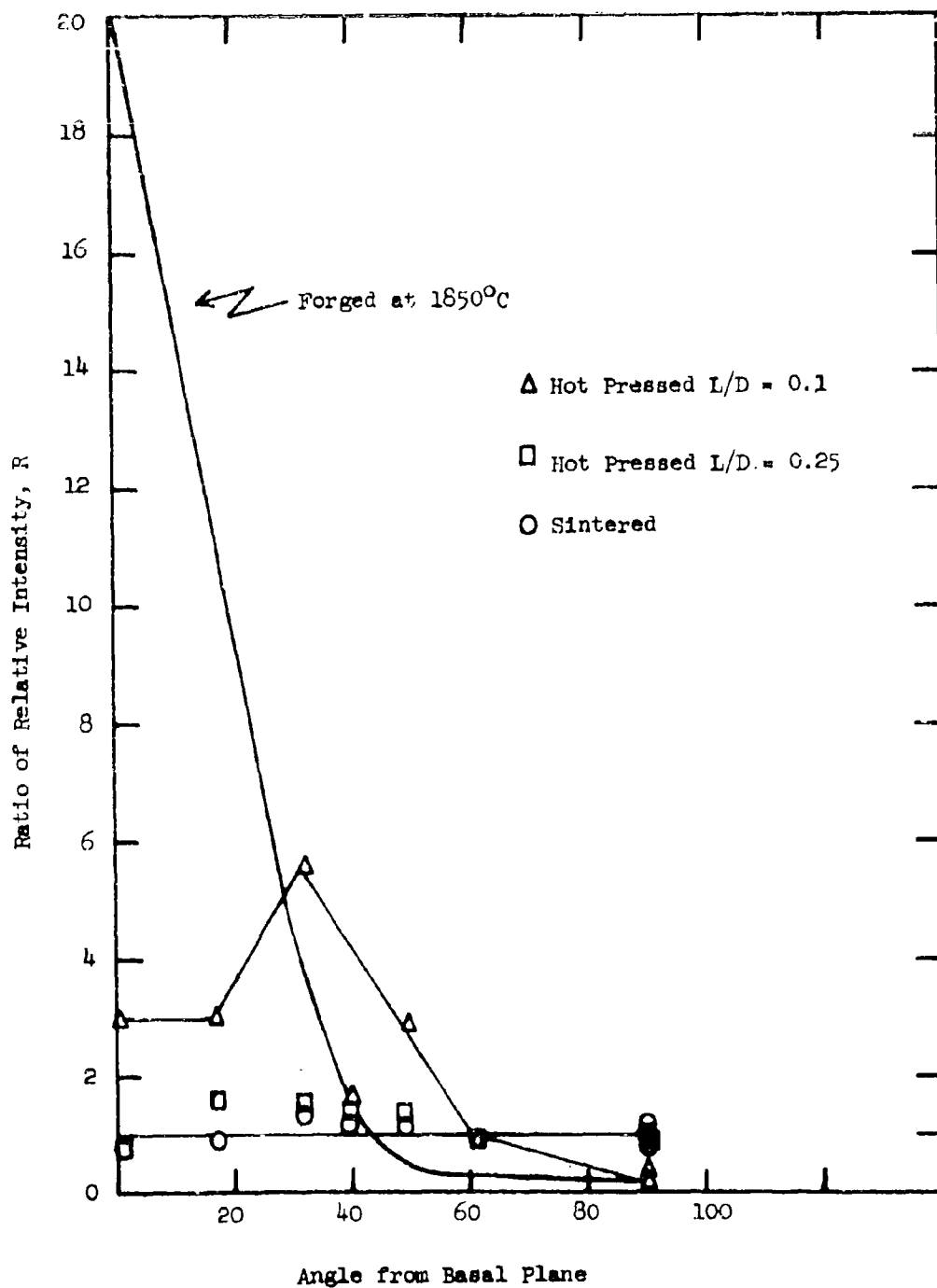


Figure 3.2 Ratio of Relative X-ray Intensity for Forged, Sintered and Hot Pressed  $\text{Al}_2\text{O}_3$ .

the cycle. This kept the powder column in contact with the die wall throughout the cycle in contrast to forging and nominally resulted in a hydrostatic pressure condition within the die. The thick sample (4-inch diameter by 1 inch high) exhibited essentially a constant  $R$  value of 1 indicating no preferred orientation. The hot pressed sample having a lower  $L/D$  ratio did show some orientation; however, instead of being basal the peak in  $R$  occurred at a  $\phi$  equivalent to the  $(0,2,2,10)$  plane. The Lucalox (sintered) material gave a constant  $R$  value of one indicating, of course, no preferred crystallographic orientation.

The lack of orientation in the sintered and hot pressed samples is expected if a random distribution of crystallite orientations is present in the powder compact and diffusional processes provide the major densification mechanism. The current view<sup>17,18</sup> of both hot pressing and sintering would predict such a result. Thus, the occurrence of orientation in the low  $L/D$  hot pressed sample was surprising. The low powder column height may have allowed shear and bending moments to exist within the powder mass which would promote non-diffusional processes, e.g., grain boundary sliding or dislocation plastic flow. Slip on a preferred slip system usually accounts for preferred orientation, thus this result certainly suggests that slip can occur in hot pressing. Another surprising feature of this result is the fact that a non-basal (the preferred slip system) orientation was found. It is uncertain how much emphasis to place on this finding as the orientation found may be more a reflection of the stress condition in the billet rather than the slip system involved.

## 2. High Density Forging

The first five forgings in Table 3.1 were conducted with the goal of obtaining uniform high densities. Billets 1189 and 1191 were forged under nearly identical conditions. The billets were compared and then No. 1191 was placed back in the die and reformed and held for 4 hours at 1880°C under pressure. The grain size was a uniform equiaxed 17 microns after the initial forging, and after the second forging there was a slight microstructural texture in the center of the billet with a  $16 \times 20 \mu\text{m}$  grain intercept and an equiaxed  $23 \mu\text{m}$  grain intercept at the periphery. The equiaxed structure certainly corresponds with a recrystallized structure. The fact that little grain size difference was noted after the second four-hour hold at temperature suggests that continued recrystallization occurred during this long hold. For 210 minutes of the hold period no macroscopic deformation was detected (dial gage monitor system) thus, the apparent continuance of the recrystallization was somewhat surprising. The reformed sample was denser ( $3.985 \text{ gm/cm}^3$  to  $3.980 \text{ gm/cm}^3$ ) which suggests that pore removal continues either by normal diffusional processes operative in sintering or perhaps by the mechanism previously suggested<sup>15</sup>; nucleation of the new set of grains on pores which had been isolated from the boundary. This places the pores on a grain boundary where they can be effectively eliminated by the normal diffusional processes.

Billets 1222 and 1232 were forged from presintered starting compacts into four-inch diameter dies. The lateral flow was markedly greater than the earlier forgings (three-inch dies). Consequently, the fractional effects

were greater and dome shaped billets resulted. Both forgings contained sizable opaque zones and were not analyzed in detail.

### 3. Influence of Temperature on Forging

The series of forgings at varying temperatures were all "powder" forgings using Grace  $Al_2O_3 + 0.1\% MgO$ . The  $MgO$  additive was desirable because previous work had shown that  $MgO$  retarded recrystallization and resulted in more uniform microstructure than if  $MgO$  was absent. Whether or not recrystallization is inhibited is probably still open to question. The final load was kept constant (5000 psi assuming full expansion in the die cavity). Time at temperature and pressure were held to within the 35-60 minute range as it was desired to have some fine-grained billets among the group and a better assessment of the influence of temperature could be gained by holding time relatively constant.

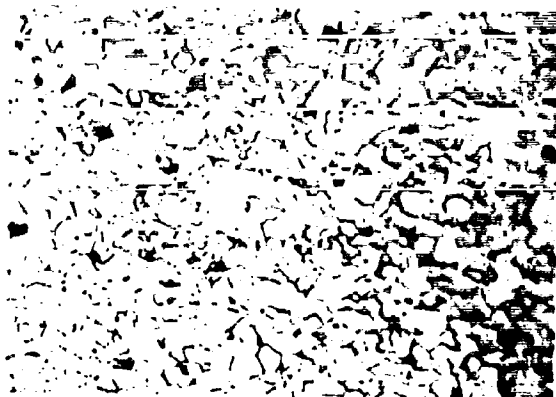
The microstructures were quite uniform throughout three of the billets in contrast to many other forged  $Al_2O_3$  billets. This was attributed both the uniformity of the deformation with the present lubricant system deformation cycle, etc., and the  $MgO$  additive which seems to influence grain development. Representative microstructures for the three forging temperatures are shown in Figure 3.3. A density difference was noted among the three forgings as well as the grain size differences. Both properties are shown in Table 3.2.

It was interesting to note that both the 1650°C and 1850°C forging (Figure 3.3 a and c) exhibited an equiaxed microstructure while the first 1740°C forging, D1240, exhibited a pronounced microstructural texture. The second forging in this temperature range was conducted only 10°C higher (1750°C), but the structure (Figure 3.4) was decidedly less uniform than any of those shown in Figure 3.3. Also, there was a mixture of three grain morphologies; large (20  $\mu m$ ) equiaxed grain, medium (10-20  $\mu m$ ) oriented grains and small (< 5  $\mu m$ ) equiaxed grains.

Before discussing the implications of the grain size and shape, the crystallographic orientation data for these samples will be presented.

Figure 3.5 illustrates the crystallographic orientation of Sample 1277 forged at 1850°C. The orientation was determined for two samples each at a different distance from the center of the billet. The results show that the degree of basal orientation decreases radially from the center of the billet to the outside. This condition has been found for most billets. No. 1282 forged at 1650°C exhibited this condition as well as a number of billets tested last year.<sup>6</sup> Sample 1297 forged at 1750°C showed almost equal values of R for both center and rim sections. The tendency for a stronger basal orientation in the center section is probably due to the higher bending moment in this region. The bending moment is the origin of the rotation of the crystals by basal slip to a direction normal to the pressing direction.

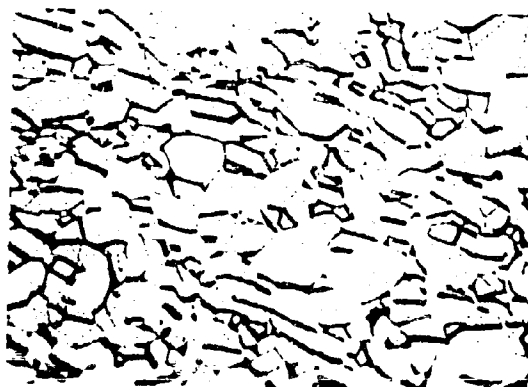
The degree of orientation for samples forged at the three temperatures is shown in Figure 3.6. The percent reduction was identical



#5181-14

a

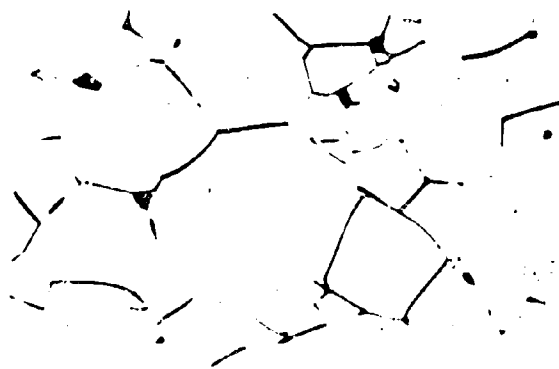
500X



#5145-1

b

500X



#5181-8

c

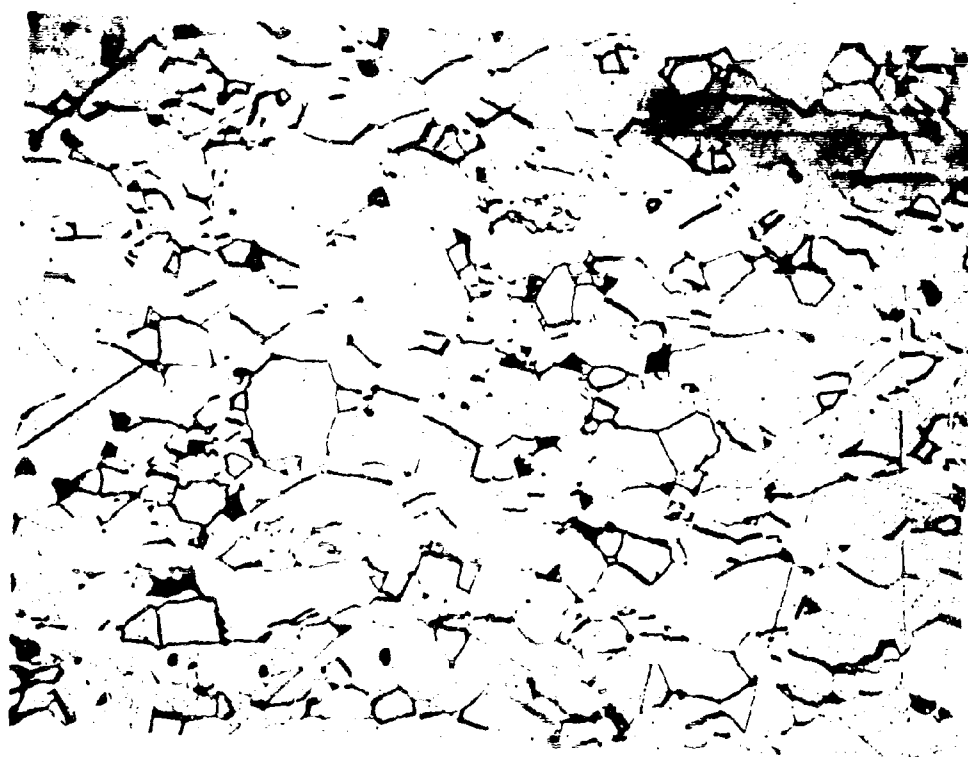
500X

Figure 3.3 Powder Alumina Forgings at a) 1650°C - D1282, b) 1740°C - D1240 and c) 1850°C - D1277.

TABLE 3.2

MICROSTRUCTURE VARIABLES ON BILLETS FORGED AT VARYING TEMPERATURES

<u>Forging Temperature</u>	<u>Billet No.</u>	<u>Density gm/cm<sup>3</sup></u>	<u>Grain Intercept Microns</u>
1850	1282	3.978	4.3
1740	1240	3.985	6.5 x 8.7
1750	1297	3.972	mixed 4 to 20
1850	1277	3.986	21



#5194-1

500X

Figure 3.4 Microstructure of Several Powder Alumina Forgings at 1750°C.

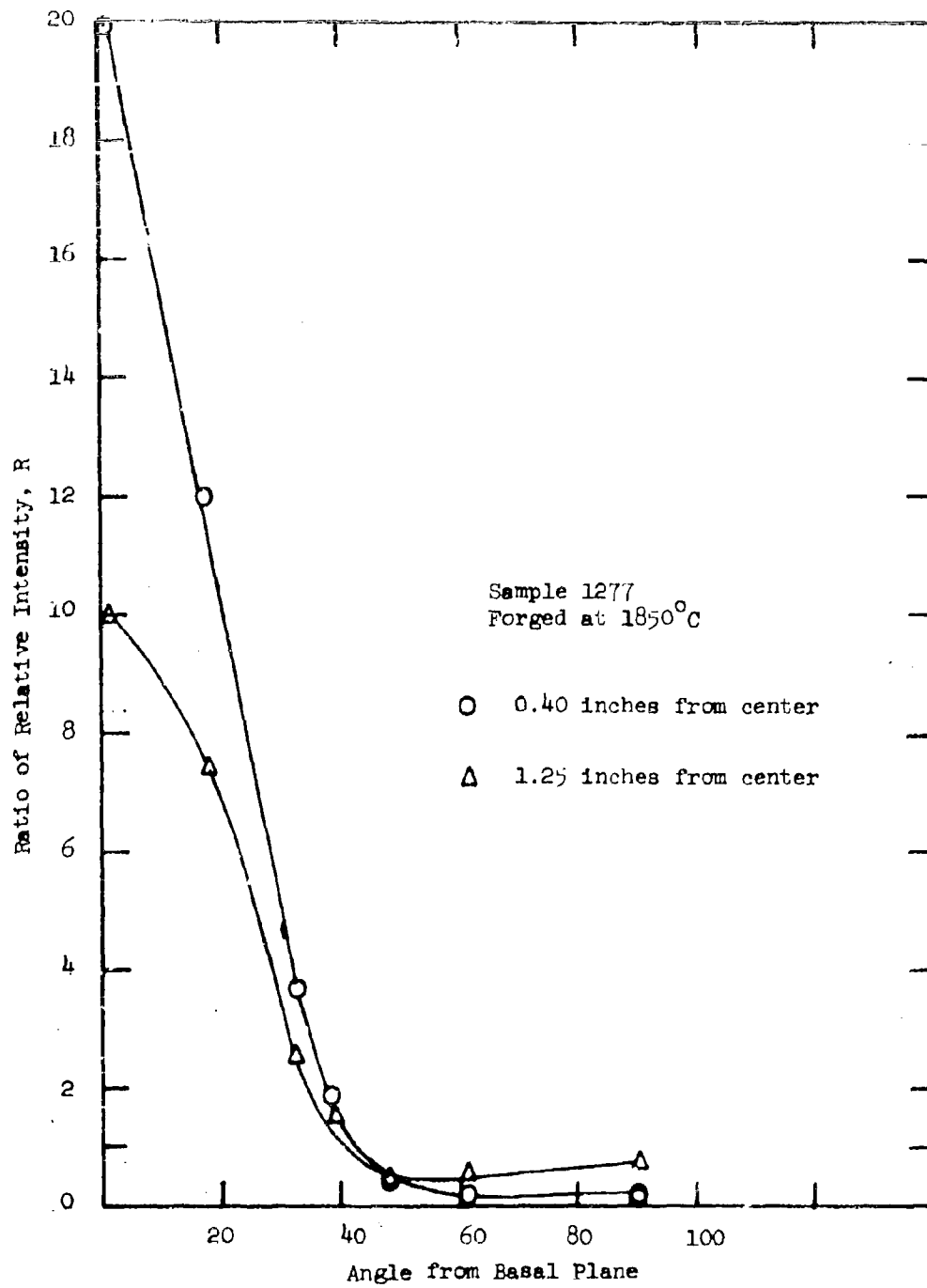


Figure 3.5 Ratio of Relative X-ray Intensity at Center and Rim Position of Forged Billet.

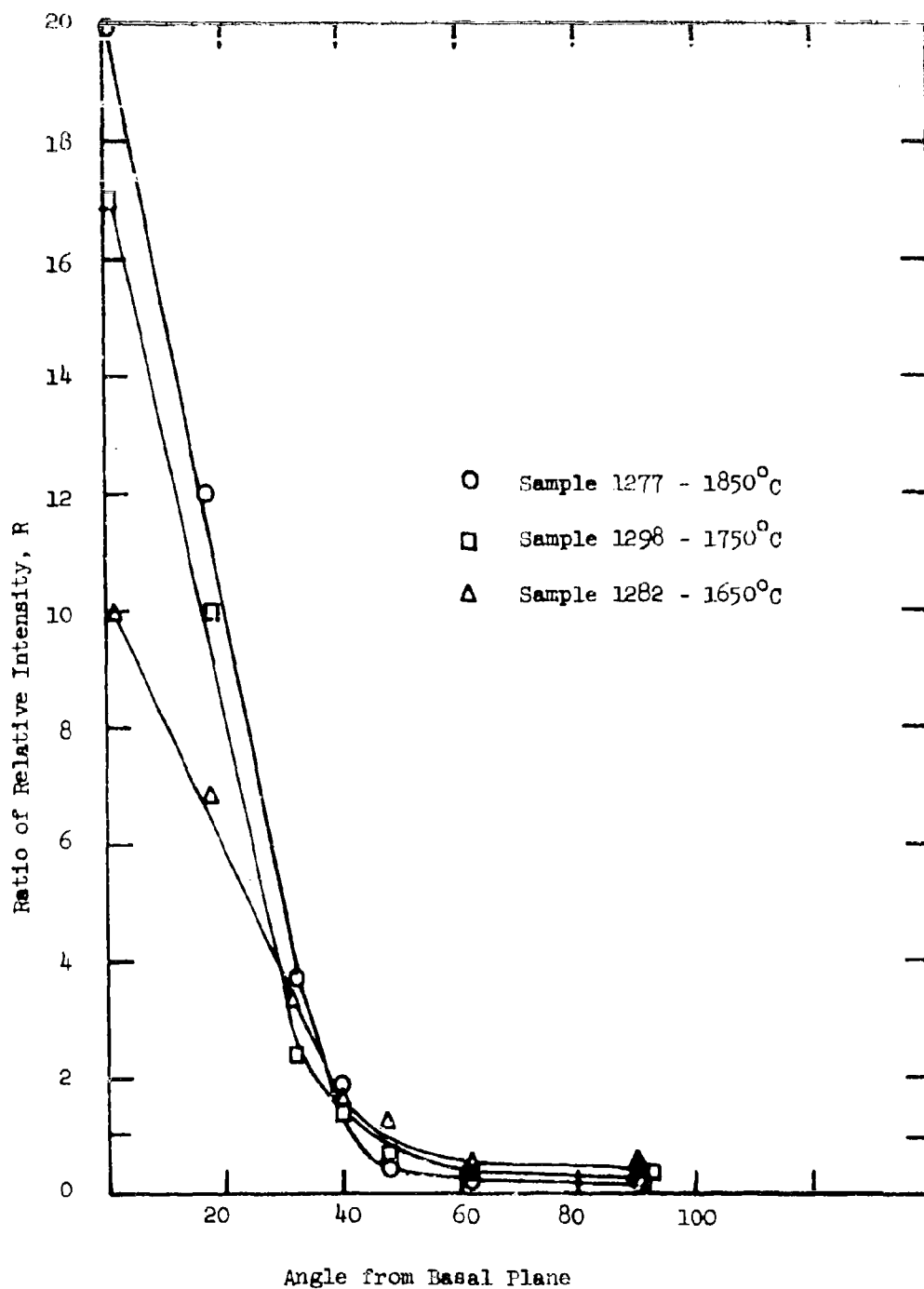


Figure 3.6 Ratio of Relative X-ray Intensity for Billets Forged at Three Different Temperatures.

within experimental error for the three forgings. Only data from the center section (center of piece examined 0.4 inches from center of billet) is plotted. The degree of orientation increases with increasing forging temperature. Slip is an activated process, thus it becomes easier with increasing temperature. Consequently, it is quite reasonable to expect that higher forging temperature (keeping forging pressure constant) would result in more grain rotation by basal slip. This also implies that secondary slip systems (prismatic and rhombohedral) do not increase in importance in forging as temperature is raised. Also, the increased starting grain size with increased forging temperature would favor deformation by basal slip as opposed to boundary sliding creep which, of course, would not produce orientation.

The four micrographs presented represent almost the complete range of microstructures observed in forged  $Al_2O_3$ . The interpretation and implications in view of the texture are as follows:

Forging at 1850°C - The crystallographic texture found demonstrates that basal slip provided the main deformation mode. Figure 3.3 c shows an equiaxed structure suggesting that rapid grain growth either after recrystallization or due to strain enhanced grain growth gave a uniform grain size. Preferred growth directions which occasionally produce coarse tabular grains in  $Al_2O_3$  are not important. The earlier view<sup>10</sup> was that this was a recrystallized structure and there is no evidence to suggest that it is not although the possibility of strain enhanced grain growth is at least mentioned.

Forging at 1750°C - Again, the billets possessed crystallographic textures demonstrating the dominance of basal slip. Figure 3.3 b shows a strong microstructural texture. One interpretation of this structure is that it represents a deformation structure caused by the elongation of the grains due to basal slip. A second interpretation again postulates orientation by basal slip, but then the elongation became enhanced due to differing growth rates for the various crystallographic orientations. The final structure would still be a deformation structure but the degree of texture would be more a function of time at temperature rather than percent deformation. The second structure (Figure 3.4) obtained under similar 1750°C forging conditions looked quite different. The elongated grains appear similar to the deformation structure shown in the first 1750°C forging. Also, apparent in this micrograph are fine (2  $\mu m$ ) grains, and it is thought that these are recrystallized grains. (The grain size is about 1  $\mu m$  at the start of the forging cycle and about 5-20  $\mu m$  at the end of the deformation part of the cycle.) Some of the grains present are both equiaxed and larger than the elongated grains. It is thought that these result from rapid grain growth of the recrystallized grains. Thus, this one micrograph



shows the deformed grains, the fine recrystallized grains and the coarse recrystallized grains.

Forging at 1650°C - Again, the x-ray results show crystallographic texture. However, a fine nearly equiaxed grain structure (Figure 3.3 a) results. The fact that it is equiaxed suggests that it recrystallized, but the question arises as to why the 1750°C forging still exhibited a deformation structure. One possible answer is that at 1650°C strain energy is more easily built up due to lower rates of annihilation and boundary migration than at 1750°C. The higher strain energy would promote the early occurrence of recrystallization. A second explanation is that GBS plays a greater role in the deformation process at lower temperature. Diffusion and grain boundary motion during continued deformation keeps the structure nearly equiaxed.

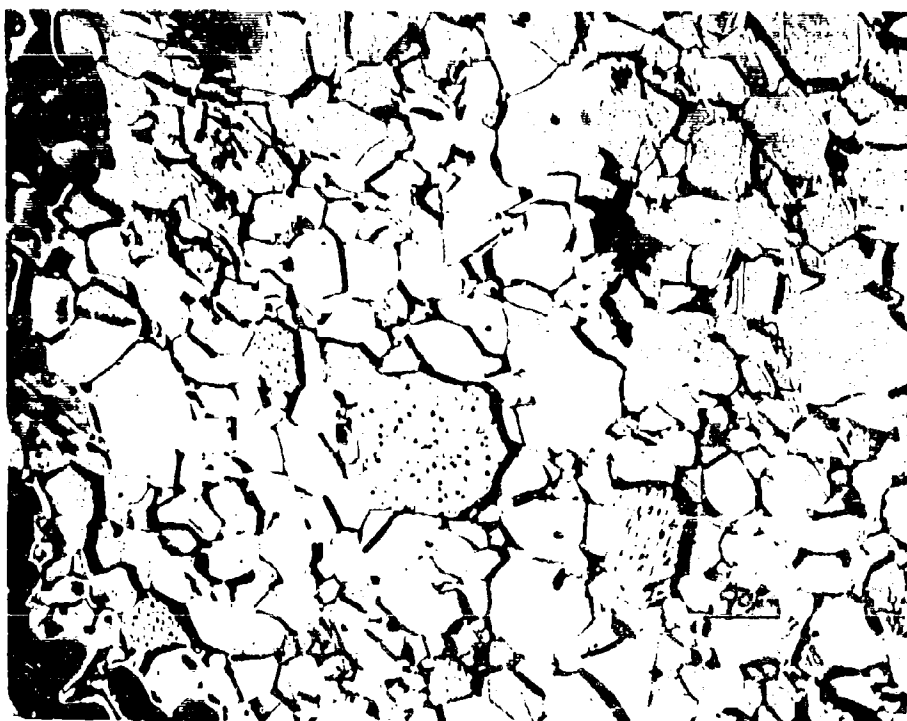
#### 4. Rapid Deformation-Quenching Experiment

Billet 1294 was forged (from a dense billet) and quenched very quickly (4 minutes total time above 1500°C once forging began). Although the billet was whole, grain boundary separation led to internal cracking and porosity in all areas except the center region in contact with the punches. Figure 3.7 illustrates an etched area in this dense region. The structure is decidedly non-uniform, thus it is difficult to say whether or not the recrystallization process was caught during the initial stages of nucleation and growth. It is suspected that the rapid deformation was too inhomogeneous to produce generalized recrystallization. Several grains show etch pit development. It is apparent that these grains were favorably oriented for etching; however, it is unclear whether or not these pits are the termini of dislocations. The pits in the large grains do appear to have some line orientation which does not correspond with polishing scratches on adjacent grains. As such they are suggestive of slip bands. The experiment showed that the material failed due to the rapid deformation and quenching. It also resulted in etched structures which could be interpreted as being caused by slip. This is quite reasonable in view of the deformation processes thought to be operative during forging.

#### 5. Mechanical Properties

Bend tests were conducted on billet 1277 forged at 1740°C. The grain size and density data are reported in Table 3.2. The reason this billet was chosen for testing was because it was essentially fully dense and possessed a very uniform textured microstructure. The bend test data is shown in Figure 3.8 and compared with data of Spriggs et al.<sup>12</sup> for hot pressed Al<sub>2</sub>O<sub>3</sub> at two grain sizes.

The higher 25°C strength for the forged Al<sub>2</sub>O<sub>3</sub> certainly is partially explained by the absence of stress corrosion. One test was conducted in air and this falls near the bottom of the range for the 25°C tests. The tests on hot pressed material were conducted in the ambient atmosphere which can degrade strength 20-30%. Even considering the stress



#5193-3

1000X

Figure 3.7 Microstructure in Dense Region of Rapidly Forged-Quenched Billet 1294.

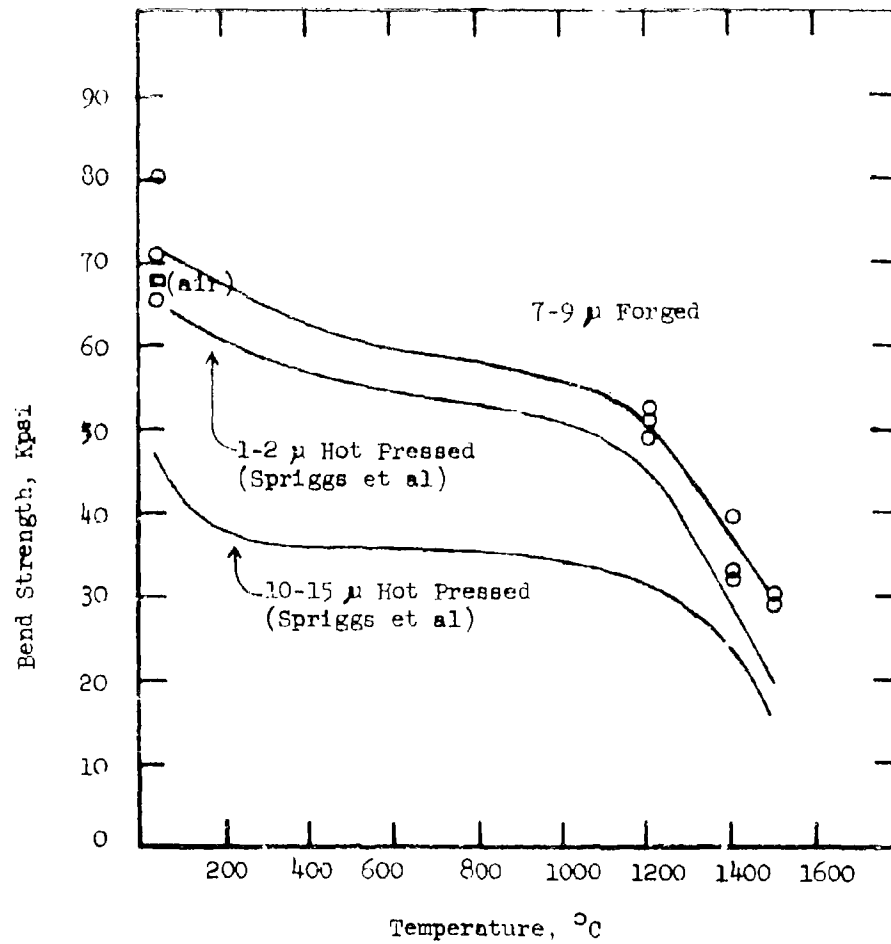


Figure 3.8 Bend Strength versus Temperature of a Forged Billet Compared to Hot Pressed Material.

corrosion factor the room temperature strength is slightly higher than that expected for material of this grain size.

The high temperature tests, should be directly comparable since atmosphere effects are not expected. The forged  $\text{Al}_2\text{O}_3$  has a grain size near the 10-15  $\mu\text{m}$  category tested by Spriggs, et al. The curves show the forged material to be considerably stronger at higher temperature.

These results could be explained in a number of ways; unfavorable orientation between maximum shear stress and the preferred slip plane in a textured sample, unfavorable orientation between tensile stress and preferred cleavage plane, long dislocation glide distances due to easy dislocation propagation across low angle grain boundaries. Grain boundary sliding may be restricted in a highly textured sample, and retained complex dislocation structures from forging may raise yield stresses for mobile dislocations.

Earlier studies on the 1350-1550°C deformation of  $\text{Al}_2\text{O}_3$  were interpreted as having both a strong diffusive and grain boundary sliding component. It was unclear what precipitates fracture, but constraint at triple points and the continuance of the above processes probably builds up local stresses until grain boundary separation occurs. This study (Section II) has shown that at high strains high purity  $\text{Al}_2\text{O}_3$  undergoes work hardening. Other recent results have shown the presence of a Bauschinger effect and other behavior usually associated with dislocation processes. Thus, it appears that 1350-1550°C flow and failure criteria in  $\text{Al}_2\text{O}_3$  are complex and probably involve mechanisms which would be affected by the microstructural and crystallographic texture of sample 1277. One or several of the potential mechanisms listed above are probably responsible for the higher strength of forged  $\text{Al}_2\text{O}_3$ .

#### D. Summary

1. Forging in the 1650-1850°C range can result in microstructure varying from equiaxed to oriented back to equiaxed with increasing temperature.
2. Recrystallization is accompanied by grain refinement rather than just coarsening by strain enhanced growth.
3. Long (4-hour) hold periods under pressure at the conclusion of apparent forging deformation apparently is accompanied by continued step-wise recrystallization as little grain size increase is noted.
4. The center of the forged billet usually has a greater basal orientation than the outer periphery.
5. The relative orientation increases with increasing forging temperature.
6. Rapid forging and quenching results in material failure by grain boundary separation and perhaps retained dislocation structure.
7. The mechanical properties of forged alumina are improved over hot pressed alumina of equivalent and even a factor of 8 smaller grain size.

#### IV. STRESS CORROSION OF MAGNESIUM OXIDE

##### A. General

Stress corrosion cracking is a well-known phenomena that is controlled by mechanical or chemical processes occurring at the interface between the solid and the environment. Under some conditions the surface reaction can be beneficial, i.e., the Joffe's effect where dissolution increased the crack tip radius thereby blunting a potential critical crack. In most cases the surface reaction degrades the usable strength and consequently, knowledge of such reactions is important for structural materials. There are two major classes of models governing the advancement of the stress-corrosion crack; 1) those which postulate crack advancement by chemical dissolution at the tip - the point of highest chemical potential and 2) those which involve only mechanical phenomena such as mobile dislocations or reduction of the surface energy term in the Griffith relationship.

Moderate strain rate testing in earlier efforts<sup>6,7</sup> on polycrystalline MgO had led to the following general conclusions; 1) Stress corrosion did not occur in MgO at room temperature at testing strain rates in the order  $5 \times 10^{-3}/\text{min.}$ , 2) room temperature fractures were nucleated by mobile dislocations; hence, high strengths were obtained in both air and argon for annealed specimens. Thus, the room temperature strength was not particularly sensitive to the initial crack length although it was not possible to say whether it was strictly due to the Griffith criteria or if the dislocation mechanism of Clarke et al<sup>22</sup> was dominant. At liquid N<sub>2</sub> temperature the mechanically polished samples which certainly contained fresh dislocations showed significantly higher strengths than surfaces with greater crack lengths. This suggested that the classic Griffith relation holds at 77°K, rather than a dislocation crack nucleation process. The most recent<sup>6</sup> study on vacuum hot pressed undoped MgO included a classic dead-load stress corrosion study in a water environment. A pronounced delayed failure curve was observed which was interpreted by the Charles and Hillig<sup>23</sup> dissolution model. However, because of the strong contention among numerous investigators (including the authors) that room temperature failure normally involves dislocation coalescence various possible mechanical models for stress-corrosion were not eliminated.

One troublesome feature of the recent study was the fact that small quantities of sodium aluminum silicate grain boundary phases were observed in the vacuum hot pressed material. This material was produced from Fisher MgO without any densification aid in pressing. The presence of a grain boundary phase made it necessary to ask whether the observed stress-corrosion was intrinsic to MgO or the grain boundary phase. Consequently, one goal of the work to be reported was to measure the delayed failure behavior of a second hopefully purer grade of polycrystalline MgO.

A second objective of the current work was to test at least one potential mechanical model of stress corrosion. Westwood<sup>24</sup> has observed that complexes of high negative or positive charge or molecules of high dipole moment significantly enhanced dislocation mobility in single crystal MgO. Thus, introduction of such species into the standard corrosion environment should alter the slope of the delayed failure curve if a mechanical corrosion model involving mobile dislocations is controlling the crack extension.

## B. Material and Procedure

### 1. Specimen Preparation

The MgO specimens tested were vacuum hot pressed under another program\* by the MgO-LiF process where 0.3 wt. % LiF was incorporated. The MgO powder used was from a different source (Baker AR) than the MgO used in the original<sup>o</sup> study (Fisher Electronic Grade). A typical cation impurity analysis is shown in Table 4.1. The Baker material is equal or lower in all cation impurities except sodium compared with the Fisher material. The transition metals are especially low in the Baker material. However, since the grain boundary phase identified<sup>o</sup> in the hot pressed Fisher material was  $\text{Na}_6\text{Al}_4\text{Si}_4\text{O}_{17}$  it is not clear that material produced with the Baker material will be void of this phase. The hot pressed sample was annealed by slowly raising the temperature to 1000°C and holding for 60 hours. The sample was very transparent, thus essentially 99.9+% dense.

The microstructure (Figure 4.1) revealed an equiaxed 20 micron grain structure. Replicas were examined in the electron microscope for evidence of grain boundary phases. Figure 4.2 illustrates a typical area and it can be seen that while some grain boundaries appear quite clean others appear to contain a grain boundary phase. Figure 4.3 illustrates such a boundary at higher magnification. Thus, it is clear that testing this material provides only a variation in the chemistry and microstructure of the polycrystalline MgO compared with the previous material, but not the pure single phase MgO desired.

### 2. Sample and Test Arrangement

The dead-load fracture tests were conducted on 0.1 inch x 0.2 inch x 1.75 inch specimens in a lever arm test frame equipped with microswitch-clock arrangement to record time to failure. A brass 4-point bend test fixture was equipped for holding liquids, and tungsten (outer) and alumina (inner) knife edges were employed. Mylar sheet was inserted between the knife edge and the specimen.

A base-line dry strength was obtained two ways; by testing the strength in liquid  $\text{N}_2$  and then machining smaller specimens from the two halves of the broken specimen for a "dry" 23°C test. This latter test was conducted by heating the specimen to 900°C in argon, holding for 1 hour, cooling to 23°C and loading the specimen without breaking the argon environment.

Distilled  $\text{H}_2\text{O}$  was employed as the standard test environment. The testing to check the mechanical model of stress corrosion was conducted with a dimethyl formamide (DMF) solution having a high dipole moment (3.8 Debye units).  $(\text{CH}_3)_2\text{NCHO}$  is completely miscible with  $\text{H}_2\text{O}$ . Westwood showed that a 1 molar solution had nearly the same effect as pure DMF on dislocation mobility provided a 400 sec delay was employed. So, samples were immersed in the 1 M DMF for 1 hour prior to loading for the dead-load fracture test.

## C. Results

The tests conducted to determine a base-line strength are listed in

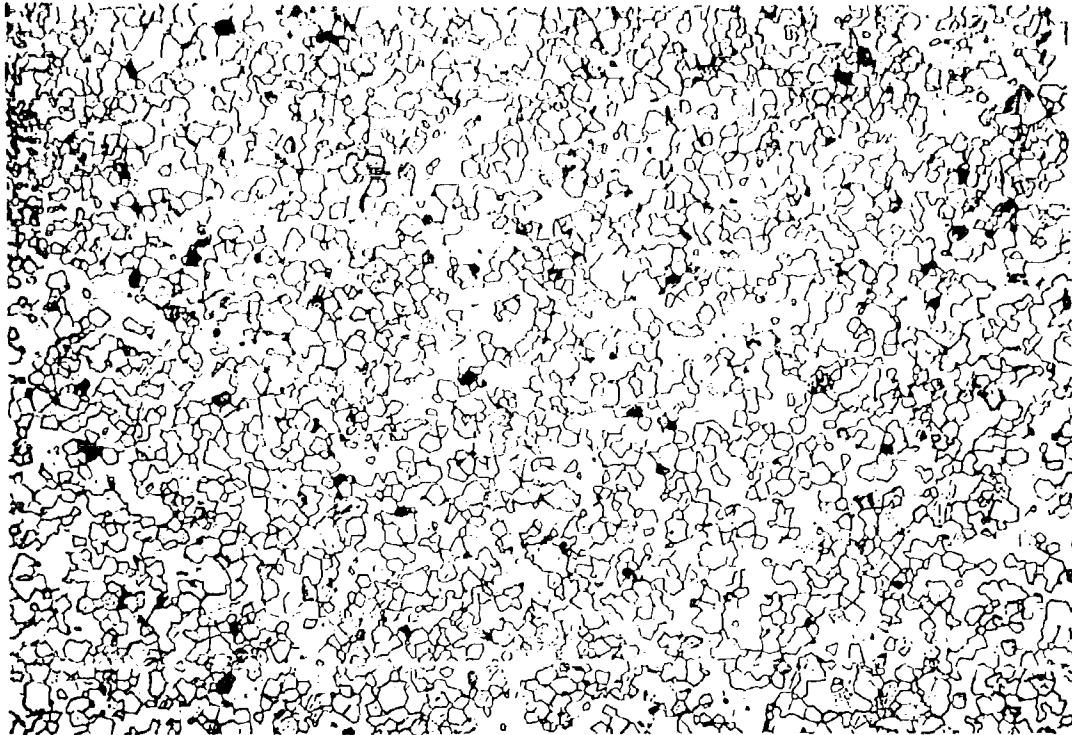
\* Development of a Manufacturing Process for Producing Optically Transparent Armor, Contract F33615-68-C-1552.

TABLE 4.1

EMISSION SPECTROGRAPHIC ANALYSIS

Manufacturer and Concentration, ppmw

<u>Element</u>	<u>Fisher Electronic Grade</u>	<u>Baker AR</u>
Na	0.001	0.100
Si	0.075	0.075
Al	0.015	0.010
Ca	0.150	0.080
Fe	0.050	0.001
Ni	0.020	0.010
Cr	0.010	N.D.



#5149-3

100X

Figure 4.1 Microstructure of Vacuum Hot Pressed Baker MgO  
using LiF Process.





#691150

1500X

Figure 4.2 Electron Micrograph of Baker MgO Sample Showing Grain Boundary Phase.



#691153

7500X

Figure 4.3 Higher Magnification View of Grain Boundary Phase in Baker MgO.

Table 4.2. The liquid  $N_2$  and argon  $23^\circ C$  tests give an average "dry" strength of  $30.3 \pm 3.3$  Kpsi.

The time to failure values for the dead-load tests are listed in Table 4.3. The stress corrosion curve is shown in Figure 4.4 where the line for the earlier<sup>6</sup> data is included for reference and comparison with the new data.

The samples were removed from the test environment as quickly as possible and the fracture surfaces replicated. The central region (half-way between the tension and compression surfaces) of the fracture surface of Sample 112-7 was void of boundary phase and any features not expected in a typical intergranular failure (Figure 4.5). Examination of the microstructure close to the tensile edge revealed several interesting secondary crack patterns on grain faces (Figure 4.6 a and b). Features such as these are not common to moderate strain rate air environment tests. Figure 4.6 a shows a semi-circular pattern which could be interpreted as intermediate stationary positions of an advancing crack front. Associated with each "rest" position of the crack front is a pattern of microcracks running normal to the semi-circular crack front. The crack pattern of Figure 4.6 b appears to run normal to and between two grain boundaries on a crack face. The connection between these cracks probably lies on an adjacent face.

Sample 112-8, also tested in  $H_2O$  was examined in detail and as with 112-7 the central region appeared equivalent to a normal moderate strain rate air environment fracture. The tensile region of the fracture was distinguished by secondary cracks associated with grain boundaries and grain faces (Figure 4.7 a and b) and even several secondary cracks associated with an area of transgranular fracture.

The comparison with the earlier data on Fisher  $MgO$  tested in  $H_2O$  is striking in that a decidedly lower stress level is needed to allow equivalent time to failures. The grain intercept of the body tested was  $20 \mu m$  as compared with  $12 \mu m$  for the body hot pressed from Fisher  $MgO$ . However, base-line strengths are used to normalize the data so the usual grain size influence is taken into account. Large grain size material for equivalent chemistries may have a higher concentration of second phases or impurity concentration due to the decrease of grain boundary area and the associated high solubility volume. However, it is thought that the differences in microstructure are not as important as the differences in starting material and manufacturing process (straight vacuum hot pressing as opposed to vacuum with the LiF additive).

The second feature of the data is the apparent effect of 1 molar dimethyl formamide. It appears that the tolerance to any dead load is reduced by this additive to the environment. As pointed out in the introduction, DMF is known to affect the dislocation mobility. Perhaps mobile dislocations (present after the machining operation) have a lower Peierls stress due to the dipole attraction (assuming the dislocation carries a charge) of the DMF. Then, at loads all the way down to  $\sim 0.6$  of the normal fracture strength dislocations rapidly move to a barrier such as a grain boundary, pile-up and finally initiate fracture. It is tempting to draw conclusions or speculate on models such as these concerning the apparent role of dislocations

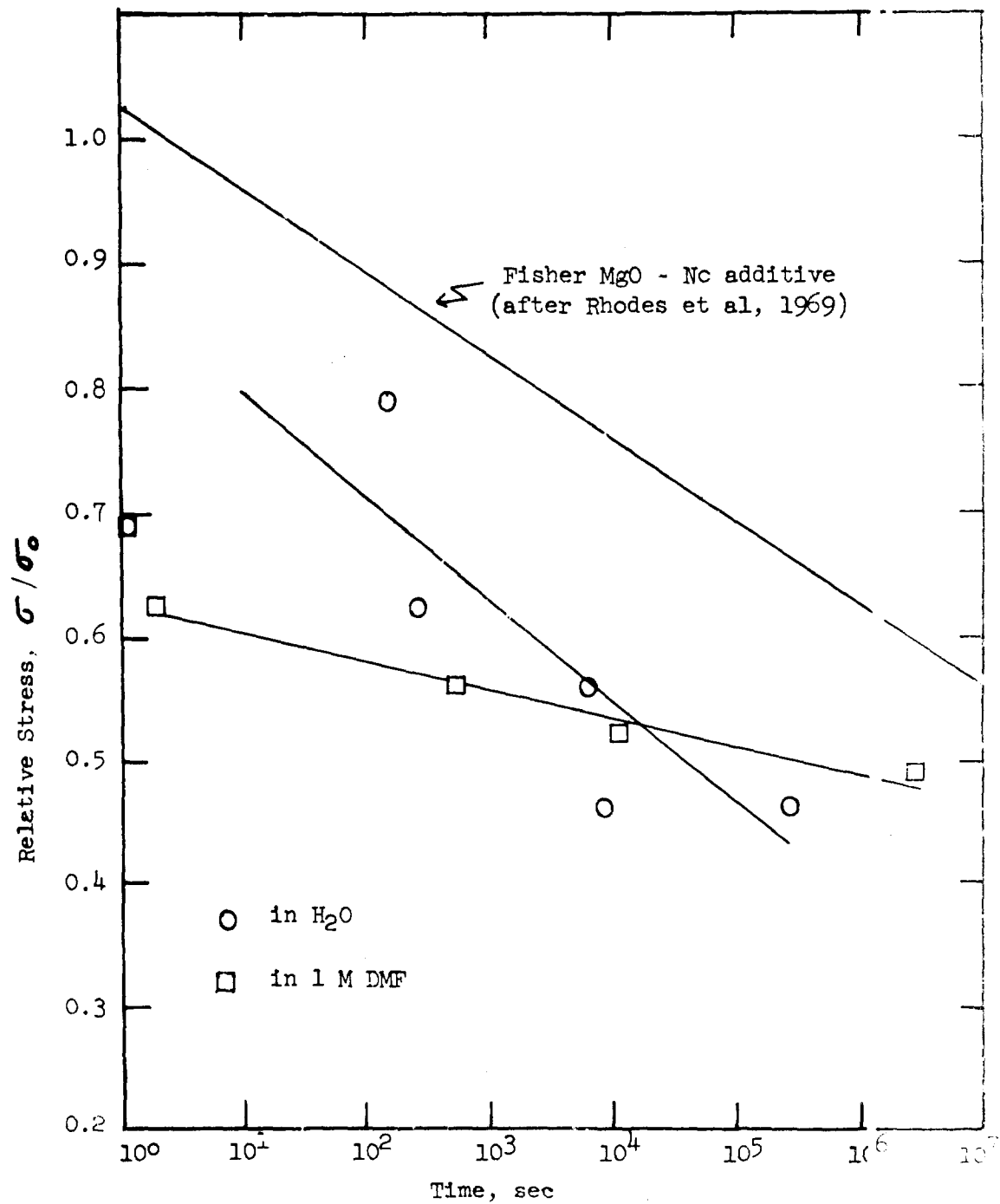


Figure 4.4 Delayed Failure Curve for Baker MgO Tested in  $H_2O$  and 1 M DMF Compared with Fisher MgO in  $H_2O$

TABLE 4.2BASE LINE STRENGTH OF MgO

<u>Specimen</u>	<u>Environment, Temp.</u>	<u>Fracture Strength, Kpsi</u>
112-1	Liquid N <sub>2</sub> -196°C	25.6
112-2	Liquid N <sub>2</sub> -196°C	31.8
112-3	Liquid N <sub>2</sub> -196°C	33.6
112-1A	Argon - 23°C	32.3
112-3A	Argon - 23°C	29.2
112-4A	Argon - 23°C	29.6
112-1B	Air - 23°C	26.5
112-2A	Air - 23°C	26.4

TABLE 4.3

DELAYED FRACTURE TEST ON MgO

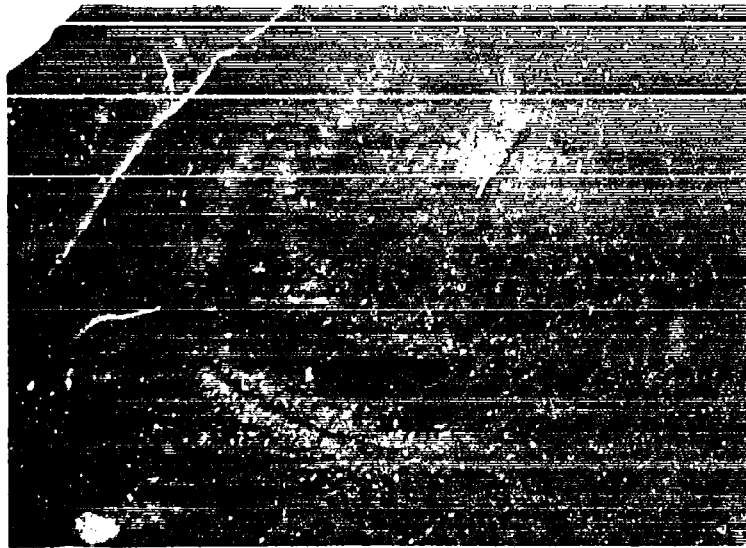
<u>Specimen</u>	<u>Environment</u>	<u>Load Kpsi</u>	<u>D</u>	<u>Time to Failure, sec</u>
112-5	H <sub>2</sub> O	24.0	0.792	$1.56 \times 10^2$
112-6	H <sub>2</sub> O	21.0	0.694	0
112-10	H <sub>2</sub> O	19.0	0.627	$2.7 \times 10^2$
112-7	H <sub>2</sub> O	17.0	0.561	$6.8 \times 10^3$
112-8	H <sub>2</sub> O	14.0	0.463	$2.6 \times 10^5$
112-9	H <sub>2</sub> O	14.0	0.463	$9.4 \times 10^3$
112-11	1 M DMF	15.0	0.496	$2.46 \times 10^6$
112-12	1 M DMF	21.0	0.694	0
112-13	1 M DMF	19.0	0.627	2
112-14	1 M DMF	17.0	0.561	$6 \times 10^2$
112-15	1 M DMF	16.0	0.528	$1.2 \times 10^4$



#691103

1500X

Figure 4.5 Central Region of MgO Stress Corrosion  
Sample 112-7.



#691109

a

7500X



#691110

b

7500X

Figure 4.6 A and B Secondary Crack and Corrosion Features on Grain Face near Tensile Surface of MgO Stress Corrosion Sample 112-7.



#691121

a

7500X



#691122

b

7500X

Figure 4.7 A and B Secondary Crack Features near  
Tensile Surface of MgO Stress Corrosion  
Sample 112-8.



in delayed failure in MgO. However, this is premature for the following reasons:

1. Some measure of the chemical corrosion of MgO by 1 M - DMF compared with H<sub>2</sub>O should be obtained.
2. The stress corrosion of MgO with a one-hour no load hold in pure H<sub>2</sub>O is needed.
3. A larger number of samples should be tested under both conditions.
4. The apparent sensitivity of the delayed fracture curve to chemistry and production technique makes generalizations about dislocation activity in stress corrosion suspect.

It is this sensitivity to chemistry and/or production technique which leads one to conclude that the behavior measured is extrinsic and perhaps more a function of impurity segregation at grain boundaries or grain boundary phases. If this is the case clearly a chemical dissolution model such as that proposed by Hillig and Charles<sup>20</sup> applies. The stress corrosion curve for the hot pressed Fisher MgO was recently<sup>6</sup> analyzed by this model and the activation volume was found to be 1.37 cc/mole and surface free energy between solid and reaction product to be 68 ergs/cc. A similar analysis of the new data could be accomplished, but again, it seems inappropriate until support for a particular mechanism is found.

The electron microscopic examination of fracture faces revealed many secondary crack features near the tensile stress surface. It is thought that many of these cracks were formed during the initial corrosion, therefore, actually preceding the catastrophic crack. This suggests that the stress corrosion activity was widespread along the fracture face and probably throughout the gage length. Thus, it appears that non-catastrophic crack growth is possible. The cracks shown in Figures 4.6 b, 4.7 a and 4.7 b give the appearance of being associated with dislocation flow or grain boundary interaction. On the other hand, chemical dissolution or temporary blunting by a second phase is a more probable explanation for the crack pattern on Figure 4.6 a.

#### D. Summary

1. Vacuum hot pressed Baker MgO made by the LiF process has less corrosion resistance in H<sub>2</sub>O than undoped vacuum hot pressed Fisher MgO.
2. The stress corrosion curve is further reduced in a 1 molar solution of dimethyl formamide in water which is known to affect dislocation mobility in MgO.
3. Secondary crack features were observed on grain faces which are suggestive of crack blunting by either a mechanical or chemical mechanism.

4. The sensitivity of stress corrosion in MgO to the type of material tested suggests that a chemical dissolution model holds yet the influence of IMF and certain secondary crack phenomena suggest that a mechanical model of stress corrosion controls. Thus, it is still not possible to unequivocally pin-point the controlling mechanism.
5. It is extremely probable that stress corrosion will operate in all commercial grades of polycrystalline MgO.

V. REFERENCES

1. K.T. Aust and J.H. Westbrook, "Lattice Defects in Quenched Crystals," edited by Cotterell et al, Academic Press, New York, p. 771.
2. A.H. Heuer and R.M. Cannon, Jr., "Elastic Deformation of Fine Grained Ceramics," presented at 15th Sagamore Army Material Conference, 1968, Syracuse University Press.
3. R.C. Folweiler, J. Appl. Phys., 32, 773 (1961).
4. S.I. Warshaw and F.H. Norton, J. Am. Ceram. Soc., 48, 499 (1965).
5. R.M. Cannon and W.H. Rhodes, "Deformation Processes in Forging Ceramics," Contract NASW-1914, Progress Report No. 1.
6. W.H. Rhodes, F.F. Jahn and P.L. Burnett, "Microstructure Studies of Polycrystalline Refractory Oxides," N00019-68-C-0108 Summary Report, June 1969.
7. W.H. Rhodes, D.J. Sellers, R.M. Cannon, W.R. Mitchell and P.L. Burnett, "Microstructure Studies of Polycrystalline Refractory Oxides," N00019-67-C-0336, Summary Report (1968).
8. J. Rasmussen, "Effect of Dopants on the Defect Structure of Single Crystal Aluminum Oxide," Sc.D. Thesis, Mass. Inst. of Technology 1969.
9. S. Timoshenko, Strength of Materials, Pt. II, 3rd edition, D. Van Nostrand, Princeton, p. 527 (1956).
10. R.M. Cannon, Jr., and A.H. Heuer, to be published.
11. R. Coble, J. Appl. Phys., 34, 1679 (1963).
12. R.E. Mistler, "Grain Boundary Diffusion and Boundary Migration Kinetics in Aluminum Oxide, Sodium Chloride and Silver," Sc.D. Thesis, Mass. Inst. of Technology, 1967.
13. D.L. Johnson and L. Berrin, "Grain Boundary Diffusion in the Sintering of Oxides," in Sintering and Related Phenomena, edited by G.C. Kuczynski, N.A. Hooton and C.G. Gibbon, Gordon and Breach, Science Publishers, New York (1967).
14. R. Chang, "Diffusion Controlled Deformation and Shape Change in Non-Fissionable Ceramics, in Proceedings of the Conference on Nuclear Applications of Non-Fissionable Ceramics, ed. A. Boltax and J.H. Handwerk, American Nuclear Society (1966).
15. R.M. Spriggs, J.B. Mitchell and T. Vasilos, J. Am. Ceram. Soc., 47, 323 (1964).

V. REFERENCES (Concl'd)

16. D.J. Sellers, A.H. Heuer, W.H. Rhodes and T. Vasilos, J. Am. Ceram. Soc., 50, 217 (1967).
17. W.H. Rhodes, D.J. Sellers, A.H. Heuer and T. Vasilos, "Development and Evaluation of Transparent Aluminum Oxide," N178-8986, Final Report June 1967.
18. A.H. Heuer, D.J. Sellers and W.H. Rhodes, J. Am. Ceram. Soc., 9, 468 (1969).
19. A.H. Heuer, W.H. Rhodes, D.J. Sellers and T. Vasilos, "Micro-structure Studies of Polycrystalline Refractory Oxides," NOW-66-0506-(d), Summary Report (1967).
20. T. Vasilos and R.M. Spriggs, "Pressure Sintering of Ceramics," Prog. Cer. Soc., 4, 95 (1966).
21. R.L. Coble and J.E. Burke, "Sintering in Ceramics," Prog. Cer. Sci., 3, 197 (1963).
22. F.J.P. Clarke, R.A.J. Sambell and H.G. Tattersall, Phil. Mag., 1, 393 (1962).
23. W.B. Hillig, R.J. Charles, from High Strength Materials, J. Wiley and Sons, New York (1965), p. 682.
24. A.R. Westwood, D.L. Goldheim and R.G. Lve, Phil. Mag., 16, 505 (1967).

Unclassified

Security Classification

DOCUMENT CONTROL DATA - R & D		
(Security classification of title, body of abstract and indexing classification must be entered when the overall report is classified)		
1. ORIGINATING ACTIVITY (Corporate author)		2a. SECURITY CLASSIFICATION
AVCO Corporation Systems Division Lowell, Massachusetts 01851		Unclassified
2. REPORT TITLE		2b. GROUP
MICROSTRUCTURE STUDIES OF REFRACTORY POLYCRYSTALLINE OXIDES		
3. DESCRIPTIVE NOTES (Type of report and inclusive dates)		
SUMMARY REPORT, 25 June 1969 to 24 December 1969		
4. AUTHOR(S) (First name, middle initial, last name)		
William H. Rhoden Rowland M. Cannon		
5. REPORT DATE	7a. TOTAL NO. OF PAGES	7b. NO. OF REFS
25 June 1969 to 24 December 1969	66	24
6a. CONTRACT OR GRANT NO.	6b. ORIGINATOR'S REPORT NUMBER(S)	
F33615-69-C-0198	AVSD-0038-70-RR	
6c. PROJECT NO.	6d. OTHER REPORT NUMBER (Any other numbers that may be assigned this report)	
10. DISTRIBUTION STATEMENT		
This document is subjected to special export controls and each transmittal to foreign governments or foreign nationals may be made only with the prior approval of the Commander, Naval Air Systems Command		
11. SUPPLEMENTARY NOTES	12. SPONSORING MILITARY ACTIVITY	
None	Naval Air Systems Command Washington, D.C.	
13. ABSTRACT		
<p>Several facets of the effect of microstructure and chemistry on the mechanical properties of magnesia and alumina were studied. Comparison of the deformation properties of high purity <math>Al_2O_3</math> with a standard research grade of <math>Al_2O_3 + 1/4\%</math> MgO demonstrated high purity material possessed a normalized creep rate approximately a factor of five (5) lower and a higher strain rate sensitivity suggesting an increased importance of diffusional creep. At strains from 3-12% evidence was obtained for strain hardening, a Bauschinger effect and polygonization which suggested considerable dislocation and grain boundary sliding activity. Also, high temperature stress-strain curves showed evidence for blunting a potentially catastrophic failure event. <math>Al_2O_3</math> press forging experiments resulted in a better understanding of deformation and primary recrystallization processes. Bend tests of a uniform 8 micron grain size textured body demonstrated higher elevated temperature strength than 1-2 micron hot pressed <math>Al_2O_3</math> suggesting a real benefit from the textured structure resulting from one of a number of potential models. Dead load stress corrosion studies on polycrystalline MgO demonstrated that the shape of the stress corrosion curve was dependent on the starting chemistry and/or minor grain boundary phases. Also, the resistance to dead load was markedly influenced by the introduction of 1 molar dimethyl formamide which had been shown to affect dislocation mobility in MgO. The evidence does not unequivocally identify whether a chemical or mechanical model of stress corrosion applies, but it is clear that stress corrosion is a problem which must be recognized in commercial bodies of MgO.</p>		

DD FORM 1473

Unclassified

Security Classification

### Equality Classification

Unclassified

**Security Classification**